1-1-2011

Numerical and experimental investigation of the dynamics of ultrasound contrast agents excited at higher multiples of their natural resonance frequency

Amin Jafari Sojahrood
Ryerson University

NUMERICAL AND EXPERIMENTAL INVESTIGATION OF THE DYNAMICS OF ULTRASOUND CONTRAST AGENTS EXCITED AT HIGHER MULTIPLES OF THEIR NATURAL RESONANCE FREQUENCY

By

Amin Jafari Sojahrood

A thesis

presented to Ryerson University

in partial fulfillment of the

requirements for the degree of

Master of Science

in the Program of

Biomedical Physics

Toronto, Ontario, Canada, 2011

©Amin Jafari Sojahrood, 2011

Author's Declaration

I hereby declare that I am the sole author of this thesis.

I authorize Ryerson University to lend this thesis to other institutions or individuals for the purpose of scholarly research.

_____

Amin Jafari Sojahrood

I further authorize Ryerson University to reproduce this thesis by photocopying or by other means, in total or in part, at the request of other institutions or individuals for the purpose of scholarly research.

_____

Amin Jafari Sojahrood

Abstract

Amin Jafari Sojahrood.”Numerical and experimental investigation of the dynamics of ultrasound contrast agents excited at higher multiples of their natural resonance frequency”, M.Sc. Biomedical physics, Ryerson University, Toronto, 2011

In this work the Hoff model for microbubble oscillations was used together with bifurcation diagrams to investigate microbubble behavior for a range of the system control parameters (driving frequency and pressure, microbubble size and shell parameters). We have shown that if the microbubble sizes are optimized so that their resonance frequency is a fraction of the sonication frequency (1/3, 1/4...), above a certain pressure threshold, the microbubbles can emit higher order subharmonics at (1/3, 2/3...) of the sonication frequency. Experimental results (using Artenga and in-house made lipid microbubbles with a 25 MHz, 30 cycle pulse using 0.1-2.5 MPa pressures) showed subpopulations of the microbubbles that were able to show this behaviour by scattering ultrasound according to the theoretical predictions (e.g. having two frequency maxima for subharmonics at f/3 and 2f/3). The ring-down analysis of the natural free oscillations of these microbubbles confirmed the theoretical resonance predictions.

Acknowledgements

Table of Contents

List of Figures

Chapter 1 Introduction

1.1 Ultrasound contrast agents in diagnostic and therapeutic ultrasound

Encapsulated microbubbles are known also as ultrasound contrast agents (UCAs). They are used clinically for imaging of blood vessels or for therapeutic applications such as drug delivery. UCAs are small gas bubbles with diameters of the order of 1 to 10 μm. UCAs are encapsulated by a stabilizing thin shell (e.g., albumin or lipid) and are filled with air or with a gas with lower water solubility than air such as a perfluorocarbon (Klibanov 2002). UCAs are usually injected intravenously and traverse the lung capillaries. Then they will reach the heart and the internal organs, where imaging is usually performed. The UCA shell, designed to reduce diffusion of the encapsulated gas into the blood, can be stiff (e.g., denatured albumin) or relatively flexible (phospholipids). Because of the gas core, a UCA is highly compressible, and therefore highly echogenic.

Currently, encapsulated microbubbles are utilized in many applications such as vascular signal enhancement (Kerbel 2006), tissue perfusion imaging (Deng and Lizzi 2002), molecular imaging (Dayton and Ferrara 2002; Lanza et al. 2002), drug delivery (Liu et al 2006), sonothrombolysis (Hitchcock & Holland 2010), opening the blood brain barrier (BBB) (Meairs

and Alonso 2007) and heating enhancement in high intensity focused ultrasound treatments (Holt & Roy 2001).

When driven by an ultrasonic pulse, these small gas bubbles oscillate with a very high shell wall velocity (e.g tens to hundreds of meters per second) and can be pushed towards a vessel wall or fragmented into nanometer particles (Shin et al. 2009). Through application of a focused ultrasound beam and high pressures, UCAs can be disrupted which offers the opportunity to locally deliver a drug or gene. Moreover, higher ultrasound harmonics radiated by the oscillating microbubbles are absorbed very fast and can locally raise the temperature of the target. This temperature enhancement may be used in high intensity focused ultrasound (HIFU) treatment of tumors (Holt & Roy 2001). It is shown that when microbubbles are employed in HIFU, due to significant temperature enhancement of the target, larger tumors can be treated in a shorter duration (Yu et al. 2006). In addition, when exciting microbubbles at lower ultrasound frequencies, significant enhancement in BBB opening has been achieved. The transient opening of the BBB will aid in the delivery of drugs and macromolecules to the targets of interest in the brain without the need to open the skull (Meairs and Alonso 2007).

Because of the many applications and the intricate and complex bubble dynamics, the engineering of ultrasound contrast agents can be optimized for many different applications. UCA size and composition can be optimized for ultrasound imaging devices to map their local distribution, to enhance local drug delivery, sonothrombolysis, BBB opening and HIFU enhanced heating. The focus of this thesis is on gaining a more thorough understanding of the dynamics of UCAs for better optimizing the subharmonic detection based imaging applications of ultrasound.

1.2 Challenges of using UCAs in ultrasound imaging

One of the major steps in diagnosing a disease and monitoring the related treatment is the ability to image blood vessels and flow. For instance, the neovasculature within breast lesions has been shown to be an independent marker of cancer (Weidner et al. 1992; Gasparini et al. 1995). Additionally, the ability to visualize tissue perfusion in real time is another useful indicator of malignancy or physiological malfunction (Wiesmann et al. 2004; Miles et al. 1998). Among all the imaging modalities capable of imaging blood flow, the number of ultrasound imaging applications is increasing because of the safe, inexpensive, and portable nature of the ultrasound (Levin et al. 2004). The capability for real time ultrasound imaging is perhaps one of the biggest advantages of the ultrasound modality, and makes it an ideal imaging option for many clinical applications. "Ultrasound represents the safest, fastest and least expensive method of scanning for many types of medical diagnosis" (Stride & Saffari 2003). In addition compared to CT and MRI, the spatial and temporal resolution is higher (Cosgrove et al. 2006). This makes their application in detection of small and rapid blood flow (e.g. focal nodular liver hyperplasia) very demanding (Cosgrove et al. 2006). One of the problems with ultrasound compared with other techniques such as magnetic resonance imaging, is that the image quality is often inferior and therefore methods for improving image contrast are highly desirable (Stride & Saffari 2003). The use of microbubbles in the blood stream can significantly improve the ultrasonic images. This is because blood does not reflect ultrasound very well and cannot be clearly distinguished from the surrounding tissue. Gramiak and co-workers (Gramiak and Shah 1968) first reported the enhancement of backscatter from blood due to the presence of microbubbles. The primary reason for this enhancement is the significant change in the density and speed of sound at the surface of the bubble which results in a significant impedance mismatch. The resulted

3

enhancement in echogenicity has been used as an example in Doppler studies named "Doppler rescue" (Harvey et al. 2001). Although this increase in echogenicity is useful for Doppler studies, regions of small blood flow may not be detectable; moreover, conventional grey scale imaging as the concentration of the UCAs is too low to produce significant backscatter (Cosgrove et al. 2006).

Fortunately, due to the low density and the very high compressibility of the gas core of the UCAs, when they are exposed to ultrasound they undergo contraction and expansion exhibiting a unique nonlinear signature. Detecting the signals related to this unique signature aids in distinguishing them from the surrounding tissue. Backscatter from UCAs consists not only of signals at the insonating ultrasound frequency, but also at harmonics of the insonating frequency. Multiples of the insonating frequency of order 2, 3, 4, etc are termed higher harmonics, those of order 1/2, 1/3, etc are called subharmonics, and those of order 3/2, 4/3 etc are termed ultraharmonics (Lauterborn 1976, Eller and Flynn 1969, Neppiras 1969, Phelps and Leighton 1997). The nonlinear response of the tissue at these specific frequencies is negligible (Bhagavatheeshwaran et al. 2004) (even though there likely is nonlinear propagation of the ultrasound in the tissues (de Jong et al. 2002), which is a separate phenomenon). Therefore, forcing the UCAs to oscillate at these nonlinear frequencies and by filtering the backscattered signals to detect only these nonlinear signals, the contrast to tissue ratio (CTR) is enhanced, thereby better visualizing the tissue vasculature. Investigating new methods to improve the CTR by exploiting the nonlinear character of the bubbles is the subject of the interest of many investigations in ultrasound imaging and therapy and the main motivation of this thesis.

1.3   Methods to improve CTR

Early ultrasound imaging techniques were not able to distinguish in many cases the echoes from UCAs due to the low concentration of the bubbles resulting in the lower reflectivity compared to the surrounding tissue signal (Cosgrove 2006; Sboros et al. 2010). However, when microbubbles are insonified with a frequency close to their natural resonance frequency, they produce a significant backscatter not only at the resonance frequency, but also at higher multiples of the resonance frequency. Although the backscatter at these higher frequencies have lower intensities compared to backscattered intensity at the insonation frequency, the second harmonic may still be strong enough to be detected by the transducer with a good signal to noise ratio (SNR) and therefore may be exploited to be used for diagnostic purposes (Shankar et al. 1999; de Jong et al. 2002). By filtering the received signal and isolating the second harmonic of the backscatter signal, significant improvement in the CTR is expected; this is because only the microbubbles are producing signal at the second harmonic frequency while the surrounding tissue does not produce significant second harmonic emission. Another advantage of the using the second harmonic frequency is that it enables detection of extremely small blood vessels and regions of very slow flow which would be missed by using a conventional mode (Calliada et al. 1998). In addition, in conjunction with B-mode imaging the cardiac motion related artifacts can also be reduced (Mulvagh et al. 1996). This will enable the visualization of microbubbles in the myocardium (Mulvagh et al. 1996). The study of second harmonic imaging for better detection of UCAs began in the early 1990s (Burns et al. 1992, Schrope et al 1992, Goldberg et al 1993, de Jong et al. 1994) and has since been utilized for imaging purposes (Chang et al 1996, Forsberg et

al 1996, 1997, Shi et al 1997). The imaging technique which utilizes the second harmonic signal is called "second harmonic imaging".

Although second harmonic imaging is available in all medical scanners (de Jong et. al. 2002), it does not always result in a good CTR. This is because at higher ultrasound imaging pulse pressures (used to increase SNR) the higher frequencies associated with the nonlinear propagation of ultrasound in tissue are significant. This produces harmonic components in the propagating pulse, and therefore in the backscatter from tissue.Separating the second harmonic of the UCAs from the second harmonic of the tissue is difficult (Cheung et al. 2008). Another limitation of using harmonic imaging is that to produce a nonlinear response from the ultrasound contrast agents, a large number of cycles in the ultrasound pulse is required to generate sufficient detectible second harmonic by UCAs (Cosgrove at al. 2006). This can significantly impair image axial resolution.

Therefore other methods have been proposed with the aim of decreasing the number of the cycles and also suppressing the harmonic generation in tissue. In this regard, pulse inversion and amplitude modulation techniques use wide band pulses to retain the spatial resolution of the conventional imaging and at the same time minimizing the second harmonic generation in tissue (Burns et al. 2000, Phillips et al. 2001, Porter et al. 2003, Brock-Fisher et al. 2006). Despite the superior resolution, however, nonlinear propagation effects still limit the maximal obtainable contrast to tissue ratio (Tang and Eckersely 2006).

Another, difficulty with using these techniques which apply low pressures, is the increased effects of noise, which reduces spatial resolution (Cosgrove et al. 2006). Thus we need special approaches to minimize the effect of noise. By repeating the phase inversion sequence numerous

times, averaging can be used to improve the signal-to-noise ratio (Cosgrove et al. 2006). This method is known as power pulse inversion (PPI) (Cosgrove et al. 2006). However, multiple repetitions may improve the SNR but it will decrease the temporal resolution, therefore making the method not suitable for measuring the rapidly flowing blood.

1.4   Subharmonic Imaging

Ultrasound contrast agents not only produce helpful enhancement of backscattered signals at the harmonics of the driving frequency, but also generate significant backscatter at half the driving frequency. This frequency component is called the subharmonic frequency. Although the generation of higher harmonics in the UCA oscillations has no threshold and gradually increases with increasing acoustic pressure, , subharmonic oscillations occur only when the excitation acoustic signal exceeds a certain threshold level (Prosperetti 1977). The subharmonic emission from free gas bubbles was first studied experimentally by Neppiras (1968). Later, theoretical predictions of the conditions of existence of the subharmonics were first obtained by Eller and Flynn (1969) and later by Prosperetti (1977). The threshold pressure for subharmonic generation was found to be minimized when using a driving frequency that was twice the resonant frequency of the free bubble and the UCA (Eller and Flynn 1969; Prosperetti 1977; Shankar et al. 1999).

In an early UCA study of insonated Levovist microbubbles by Schrope et al. (1992), subharmonics of the order of 1/2 and ultraharmonics of the order 3/2 were observed. Chang and coworkers (Chang et al. 1995) acquired a Doppler power spectrum of the subharmonic response

7

of Albunex microbubbles. Later subharmonic emission of Albunex was investigated by Lotsberg et al. (1996). Shi and colleagues (Shi et al. 1997) studied the subharmonic response of a surfactant coated microbubble agent versus different transmit ultrasound pulses and found that the acoustic pressure threshold for subharmonic generation was quite different for contrast agents with different compositions.

In a comparison study between the harmonic and the subharmonic signals to increase the CTR (Shankar et al. 1998), it was found that the ratio of the intensity of subharmonic signal scattered from UCAs to that from tissue is greater than the UCA to tissue ratio at the second harmonic. Later studies have also confirmed that subharmonic signals will have a higher CTR compared to approach that utilizes the second harmonics (Shi et al. 1999; Shi and Forsberg 2000).

In addition to the mentioned early studies, recently, ultrasonic subharmonic imaging has attracted attention as an alternative for fundamental and harmonic imaging. This interest in subharmonic emission is due to the fact that nonlinear ultrasound propagation in biological tissues does not generate subharmonics at frequencies and acoustic pressures commonly used in medical imaging. Thus, the ratio of intensity of subharmonic signal from the UCA to that of the tissue is very high. Thus subharmonic imaging has a significant advantage compared to other ultrasound imaging procedures due to a very high CTR (Chomas et al 2002, Goertz et al 2005, Krishna 1999, Shi et al 1999, Shankar et al 1998, Zheng et al 2006).

The advantage of subharmonic imaging is even more pronounced in high frequency ultrasound imaging. This is because at high frequencies the harmonic generation in tissue increases significantly and methods based on 2nd harmonic detection may not work properly.

Goertz at al. 2005, have shown the clear advantage of subharmonic over harmonic and second harmonic imaging at frequencies more than 20 MHz. Because of the significant advantage in suppressing the tissue signal at higher frequencies, the investigation of how to best generate subharmonics at frequencies more than 20 MHz has attracted a great deal of interest (Goertz 2002, Goertz et al. 2003, 2004, 2005,2004a,2006b, 2007, Cheung et al. 2008, Sprague et al. 2010).

1.5   Clinical applications of subharmonic Imaging

The most mature *in-vivo* clinical applications of subharmonic imaging are for breast imaging. In order to reduce the number of unneeded biopsies, the ability to precisely and non-invasively characterize breast lesions and their vasculature is of great importance. In addition, the detection of breast lesions at early stages is vital since early detection of the cancer is a crucial factor for survival (Smith et al 2006).

It is well known that the angiogenic vasculature within lesions conveys information about the malignancy because the vascular architecture is more bifurcated and aberrant relative to healthy tissue (Weidner et al 1992, Gasparini and Harris 1995). In addition, the neovasculature within breast lesions has been shown to be an independent marker of cancer (Weidner et al 1992, Gasparini and Harris 1995). Additionally, the ability to visualize tissue perfusion in real time using contrast-enhanced ultrasound imaging can be another useful indicator of malignancy or physiological malfunction (Wiesmann et al 2004; Miles et al. 1998). Thus early and precise detection of the vascularity and flow pattern will aid in the early detection of malignancies and can be used to monitor the progress or efficiency of a treatment by imaging the changes in the vascularity and blood flow patterns. In addition, if the imaging technique is portable and safe,

continuous monitoring of the treatment may greatly help in determining the efficacy of a particular treatment and making decisions about using an alternative treatment at the early stages if the primary treatment has not been successful.

Even though it is the modality of choice for screening for early breast cancer, mammography lacks the ability to visualize the lesion vasculature, which decreases the overall specify of the technique ("65–90% of all post mammography biopsies are found to be benign" (Zonderland et al 1999, Kopans 1998)). Recent advancements in nonlinear ultrasound (US) scanning using contrast agents as an alternative tool have been shown to increase the specificity and sensitivity of diagnostic US imaging (Ferrara et al. 2000; Frinking et al. 2000; Goldberg et al. 2001). In this regard, Doppler examinations using contrast agents have improved the visualization of deep and small vessels even with low or slow flow (Correas et al. 2001). In addition this has enhanced the detection of flow within abnormal vessels because of the enhancement of the backscattered signal by the UCAs (Correas et al. 2001). However one major limitation in conventional Doppler imaging modalities is that the UCAs can produce backscatter patterns similar to conventional tissue scatterers. To improve the UCA detection, instead of the conventional Doppler, the nonlinear signals emitted by UCAs can be exploited. Harmonic imaging (HI) is one these nonlinear signatures. However, as discussed in the previous subsection for second harmonic imaging, the major disadvantage is that the tissue also produces sufficient harmonic energy to be detected by the transducer. This decreases the CTR (Frinking et al. 2000; Goldberg e al. 2001).

(a)   (b)

Figure 1.1: Gray-scale US image shows ductal carcinoma in situ (*) and cyst ⊗ visualized in their largest cross sections. Gray-scale SHI image shows both peripheral and intratumoral flow in the cancer (*), while the cyst ⊗ is essentially avascular. (Forseberg et al. 2007).

The lack of subharmonic generation in tissue and the significant subharmonic scattering produced by UCAs can be used to distinguish between tissues and vascular structures (Forsberg et al. 2000). Furthermore, subharmonic imaging may also be advantageous for scanning tissue structures located deep in tissue, because the attenuation of the subharmonics is less than the fundamental or the harmonic signals (Shi et al. 2001). In addition, the ratio of subharmonic signal intensity from the UCAs in the blood to that obtained from the surrounding tissue is greater (by about a factor of 10) than the ratio of second harmonic signal intensity from the UCAs in blood and that obtained from the surrounding tissue (Shankar et al 1998).

Subharmonic ultrasound imaging (SHI) is capable of exclusively imaging blood vessels in real time and at the same time completely suppresses the tissue signals (Eisenbrey et al. 2011a). SHI has been successfully used to estimate perfusion in canine kidneys, and the results correlated well with radiolabeled microsphere findings (r = 0.57, p < 0.001) (Forseberg et al. 2006). It has been shown that using SHI alone for breast imaging results in superior suppression of the tissue

11

signal after employing it on a commercial scanner (Forseberg et al. 2007). In a first human pilot study, 14 women with 16 biopsy-proven breast lesions (4 malignant) were imaged with dynamic cumulative maximum intensity (CMI) SHI (Forseberg et al. 2007). The area under the receiver operating characteristic curve (Az) for the diagnosis of breast cancer was 0.64 for grayscale imaging, 0.76 for mammography, and 0.78 for SHI. For dynamic CMI–SHI, the Az increased to 0.90 and this was significantly better than mammography (p = 0.03) (Forseberg et al. 2007, Dave et al. 2010).

The diagnostic accuracy of SHI can be further improved through the use of parametric imaging, in which SHI based perfusion measurements have been shown to be a better automated tool for breast lesion characterization than CMI–SHI (p = 0.002 when comparing benign and malignant lesions with SHI perfusion alone, vs. p = 0.80 for CMI–SHI alone) (Eisenbrey et al. 2011). In addition, in case of liver imaging, the feasibility of simultaneous grayscale and SHI imaging has been studied and it was shown that the ability to simultaneously visualize both imaging modes in real time would improve the applicability of SHI as a future primary clinical imaging modality (Eisenbrey et al. 2011b). Figure 1.1 shows the significant enhancement in the diagnosis of the cancer through SHI of injected UCAs.

Despite the advantages of SHI and its successful clinical and in vivo applications in the breast, kidney and liver, these studies suffer from the poor resolution of SHI. Conventional B-mode ultrasound breast scans are done using 9-12MHz ultrasound (Athanasiou et al. 2009). However, the clinical applications of SHI in breast used frequencies of 4.4 MHz with the SHI done at 2.2 MHz. Therefore this method suffers from poor lateral resolution. In addition, sufficient number of cycles (at least 4 (Chueng et al. 2008)) should be emitted to drive the bubble to produce sufficient subharmonics, thus this method suffers even more from poor axial

resolution. Any method that can use the same contrast agents and at the same time increase the driving frequency (to increase both the lateral and axial resolutions or to decrease the pulse duration required to generate enough SNR or to increase the detectability of subharmonics (CTR)) will add to the sensitivity and precision of the method. If successful, this would aid in imaging details of the vasculature of even smaller tumors may be resolved which will help in diagnosing smaller tumors and in very primary stages.

1.6 High frequency SH imaging and its drawbacks

Imaging the microcirculation is of importance for the detection of early disease and in the detailed investigation of the effects of treatment modalities. This is because, "the formation of blood vessels, through a process known as angiogenesis, is fundamental to the proliferation of healthy tissue and disease processes such as cancer" (Cheung et al 2008). Thus a safe, portable and noninvasive imaging method capable of monitoring the blood flow in the microcirculation, is of great importance in the detection of early disease (Foster et al 2000a) and the evaluation of anti-angiogenic drugs (Kerbel 2001). In addition, obtaining information about the molecular pathways involved in the tumor growth , can be of great advantage in assessing anticancer therapies (Ferrara and Kerbel 2005). This can be possible by high resolution noninvasive imaging of molecules expressed on endothelial cells using targeted microbubbles (Klibanov 2007; Rychak et al. 2007).

In this regard, high resolution imaging can be performed on small animal studies to investigate the molecular origin of human diseases such as cancer and evaluate the potential therapies. Ultimately the successful preclinical investigations can be translated into clinical applications.

Due to poor imaging resolution, ultrasound at clinical frequencies (2–12 MHz) is not suitable for imaging the microcirculation. High frequency ultrasound above 15 MHz provides images with superior resolution (e.g. 50 μm at 50 MHz). Such a high resolution can provide insight into the spatial distribution of blood flow at a microvascular scale. This has contributed to significant advances in the area of small animal preclinical imaging in the last decade. In addition, high-frequency color flow imaging systems (Kruse et al. 1998, 2002) and integrated (Pulsed wave Doppler) PWD/color flow systems (Kruse et al. 2000; 2003) have been investigated in skin, eyes, and superficial tumors.

Although through employing high-frequency Doppler ultrasound spatial resolution and sensitivity to flow in microvessels is improved, however, the detection process can still suffer from low signal to noise ratio and tissue motion. This is because, when imaging the microvasculature, the blood velocities are very slow (mm/s to sub mm/s) and the vessels are a fraction of the imaging sample volume. They may also be at perpendicular orientations with respect to the beam axis. The applicability of these techniques is even more difficult when imaging slow blood flow near large, quickly moving vessel walls (known as the "wall thump" artifact in Doppler ultrasound (Zhang et al. 2004)).

It is possible that the use of contrast techniques may improve blood detection at high frequencies, using either B-scan or Doppler-based techniques. In addition, targeted contrast agents are proposed for emerging applications (Lanza et al. 2001). However, at high frequencies the enhancement due to microbubbles is decreased relative to the tissue. This is because most of the bubbles are off resonance and only very small bubbles are resonant at higher frequencies (and the scattering efficiency decreases at higher frequencies). Therefore there is a need to explore the nonlinear behavior of the microbubbles as a potential method to compensate for these

14

shortcomings. SHI based imaging techniques have been successfully implemented due to the increased tissue harmonics as a result of nonlinear propagation.

Subharmonic imaging is an alternative attractive choice, as the subharmonic is unique to microbubbles and cannot be created through nonlinear propagation in tissue. This may enhance the suppression of the signal from the surrounding tissue below the noise floor. The feasibility of high frequency subharmonic imaging has been demonstrated in preliminary vivo implementations in mouse and rabbit models (Goertz et al 2005). In that study the subharmonic (SH) signal from the commercially available contrast agent Definity™ showed the highest contrast- to-tissue ratio (CTR) of all the investigated nonlinear frequency components (ultraharmonics,second harmonic) (Goertz et al. 2005a). In an in vivo study performed in an arteriole of a rabbit ear, Needles and coworkers (Needles et al. 2008) found that the ability to suppress tissue signals using SH signals may enable the use of higher frame rates. Higher frame rates will improve the sensitivity to microvascular flow or slow velocities near large vessel walls by reducing or eliminating the need for clutter filters (Needles et al. 2008). Figure 1.2 depicts the significant advantage of SHI at higher frequencies compared to harmonic and fundamental imaging. Despite the advantages in suppressing the signal from the tissue, axial resolution is degraded in subharmonic imaging due to the relatively long pulse required to generate the subharmonic signal. Therefore, imaging methods that can potentially increase the axial resolution and/or sensitivity are desired.
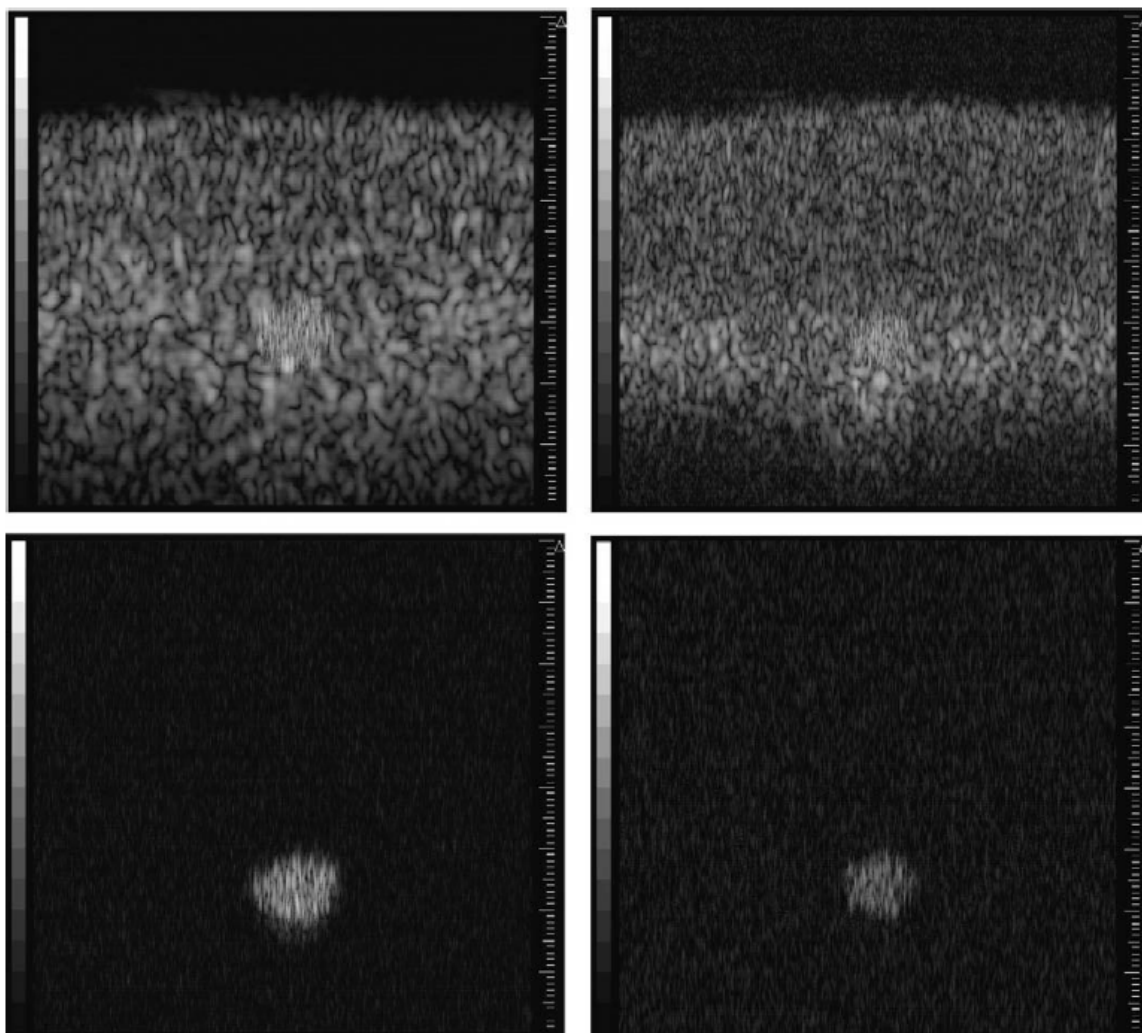
Figure 1.2: Example B-scan images of a 1-mm wall-less vessel phantom in fundamental 20 MHZ (FN20) (top left), harmonic 40 MHz (H40) (top right), subharmonic 10 MHz (SH10) (bottom left), and ultraharmonic 30 MHz (UH30) (bottom right) imaging modes. Both FN20 and H40 images show poor contrast between the vessel and tissue regions. However, SH10 and UH30 imaging suppresses the tissue signal to below the noise floor. Transmit settings are six cycles and −6 dB transmit amplitude. The images are 8 mm × 8 mm, and the spacing between the large hash marks on the vertical scale is 1 mm (Goertz et al. 2005).

1.7 Higher order SHs

In addition to subharmonics of order ½, bubbles may also generate subharmonics of higher order: 2/3, 3/4,... (n-1)/n, where n = 3,4,5… . Biagi and co-workers (Biagi et al. 2005) studied the free gas bubble behavior exposed to ultrasound, as a basic step in understanding contrast agent dynamics. They studied free gas bubble oscillations experimentally using a high frame-rate imaging system. They found that different orders of subharmonics (1/5,1/4,1/3 and 1/2 order appear during bubble dissolution. Their simulated results suggest that, for a given excitation frequency, the subharmonic order is related to the bubble resonance frequency, which in turn is determined by the bubble dimensions: "larger bubbles exhibit lower resonance frequency and thus smaller subharmonic order". In addition in an earlier experimental study on acoustic cavitation noise by Lauterborn (Lauterborn et al. 1981) the generation of higher order subharmonics of up to f/8 was observed. In that work the occurrences of subharmonics were through successive generation of period two oscillations (successive period doubling)rom subharmonics of ½ order to1/4 and then 1/8 order.

The existence of higher order subharmonics has been shown for free bubbles. However, a rigorous study of the higher order subharmonics for shelled ultrasound contrast agents has not been performed. Therefore, it is possible that through careful optimization of bubble size, pressure and the sonication frequency, direct generation of subharmonics of higher order for UCAs can be achieved.

1.8 Hypothesis and objectives

Despite the preliminary studies on free bubbles which reported the generation of higher subhrmonics (Lauterborn et al. 1981; Biagi et al. 2005) (all of which were done in low frequency range, below 5 MHz), there is no experimental or theoretical study which investigates the generation of higher order subharmonics with ultrasound contrast agents and for higher frequencies. As the generation of higher order subharmonics may enable ultrasound imaging with superior SNR, CTR and resolution, in this study the behavior of the UCAs is studied in detail in an attempt to better understand on the nature and the necessary conditions for the generation of higher order subharmonics for UCAs. However, the equations that describe the bubble oscillations are highly non-linear and there are many physical parameters in these equations that are not well known. This makes sampling the relevant parameter space to identify these conditions through typical parametric numerical analysis difficult and time consuming.

The hypothesis is of this work is that through the use of bifurcation diagrams, the conditions required for the generation of higher order subharmonics for UCA in high frequency imaging can be identified. To investigate the validity of the numerical predictions, experiments using dilute polydisperse solutions of bubbles (but extracting the signals from single bubbles) will be used.

Chapter 2 Methods

2.1 Introduction

This study has both numerical and experimental contributions. To study the dynamics of microbubbles oscillations, numerical simulations of the Hoff model for UCAs were combined with the use of bifurcation diagrams to permit the effective visualization of the results for a wide range of control parameters. Theoretical predictions of the model were studied experimentally by analyzing the signals scattered from single UCAs through sonication a polydisperse population of two different makes of UCAs. The verification of the results is done through analyzing the frequency response, the period of the bubble oscillations and finally through analyzing the ring down oscillations to estimate the resonance frequency of the considered UCA. The theoretical and experimental methods are described in the next sections.

2.2.1 Theoretical Model

The UCA oscillations are studied using the Hoff model (Hoff et al. 2000). The model is developed for viscoelastic thin shelled bubbles and is the simplification of the Church model (Church et al. 1995) for bubbles with a shell thickness which is much smaller than the bubble radius. The model describes the radial oscillations R of the bubble as a function of time and is given by equation 1:

$$\rho_L(\ddot{R}R + \frac{3}{2}\dot{R}^2) = P_0 \left((\frac{R_0}{R})^{3\Gamma} - 1 \right) - p_A(t) - 4\mu_L \frac{\dot{R}}{R} -$$
$$12\mu_s\Theta \frac{R_0{}^2}{R^3}\frac{\dot{R}}{R} - 12G_s\Theta \frac{R_0{}^2}{R^3}(1 - \frac{R_0}{R})$$

$$(1)$$

where R_0 is the initial radius, ρ_L is the density of the liquid, P_0 is the equilibrium pressure inside the bubble, Γ is the polytropic exponent, μ_L is the viscosity of the surrounding liquid, μ_s is the shell viscosity, Θ is the shell thickness and G_s is the shear modulus. $p_A(t)$ is the driving acoustic pressure and is given by equation 2:

$$p_A(t) = P_A\sin (2\pi ft) \qquad\qquad (2)$$

Where P_A is the amplitude of the acoustic driving force t is time and f is the frequency. Equations 1 and 2 were solved numerically using a 4th order Runge-Kutta as described in (Behnia et al. 2009a;Behnia et al. 2009b, Behnia et al. 2009c). The simulations were run on a computer with Intel(R) Core(TM)2 Duo 2.93 GHz CPU and 3.25GB and depending on the range of the parameter space and the sampling points would typically take 20-40 seconds to generate the solution for the radial oscillations R(t) (Figure 2.1) and 10 minutes to 3 hours to generate a typical bifurcation diagram (Figure 2.2).

Upon solving equations 1 and 2 for R(t), the backscattered pressure was calculated using equation 3 (Hilgenfeldt et al. 2000):

$$P_s = \frac{\rho R}{d} \left(2\dot{R}^2 + R\ddot{R}\right) \qquad\qquad (3)$$

Where d is the distance from the center of the bubble. For simplicity, the pressure was calculated at a distance of 1 m as in (Kvikliene et al. 2004). The fast Fourier transform of the backscattered pressure was analyzed for the frequency content. Simulations were performed for bubble sizes (diameter) ranging from 1 to 10 μm, shell thickness of 1 to 15 nm and shear modulus of 8-200 MPa. The values represent a range of published values for UCAs. For the acoustic driving force in equation 2, frequencies of 4 to 60 MHz and driving pressures of 0.01 to 8 MPa were used. The simulated acoustic insonations to generate the bifurcation diagrams consisted of 80 cycles. In addition, in case of the frequency analysis of the selected signals, 30 cycles were employed in the simulations. As the dynamics of the microbubble oscillations was the subject of this study, long pulses (narrow band mono-frequency signals) were employed. This gives better separation between the frequency components of the backscattered signals. This separation of the frequency components will also be useful for the experimental validation of the theoretical predictions.

2.2.2 Complex dynamics of the bubble model

It has been shown, both theoretically and experimentally, that the dynamics of the bubbles (free and encapsulated) are nonlinear and complex (Lauterborn et al. 1984, 1987, 1988; Parlitz et al.1990; Leighton et al. 1997; Simon et al. 2000, Behnia et al. 2009a, 2009b, 2009c,Macdonald et al. 2006) This includes higher order nonlinear UCA emissions at higher harmonics,

subharmonics and bubble destruction. Due to the lack of knowledge of the physical parameters of the bubble (e.g. shell parameters) and the complexity of the system resulting from the interaction of several control parameters (initial radius, frequency, pressure and shell parameters), it is difficult to efficiently sample the parameter space to provide an insight into the bubble dynamics. The bifurcation diagram enables us to visualize the bubble behavior in a wide range.

2.2.3 Bifurcation diagrams

A bifurcation diagram is calculated by the examination of the oscillatory response of a bubble to acoustic insonation. The left-hand column in Fig. 2.1 illustrates the normalized radius–time oscillations, after the bubble begin stable oscillations, for a 2 μm radius bubble with typical values of Gs=50 MPa, shell thickness of 3 nm and shell viscosity of 0.706 Pa.s, driven at f = 2.4 MHz. The right-hand column illustrates the corresponding frequency domain of the oscillations in the left-hand column. As seen for the oscillatory response, the radial oscillations has been normalized by the initial bubble radius while the x-axis shows time in terms of periods of the driving frequency (T = 1/f). Descending from the top of the figure to the bottom corresponds to increasing the driving pressure amplitude of the transmitted pulse to 200, 325, 377, and 500 kPa. As the driving pressure increases, the radial oscillations of the bubble become more and more nonlinear while the maximum oscillation amplitude increases. In Fig. 2.1(a), the red circles identify the value of R(t) (radial oscillation amplitude at time t), at the end of each driving period. As seen the bubble repeats the same pattern after every time interval of T seconds. This behaviour manifest a period-1 oscillation.

22
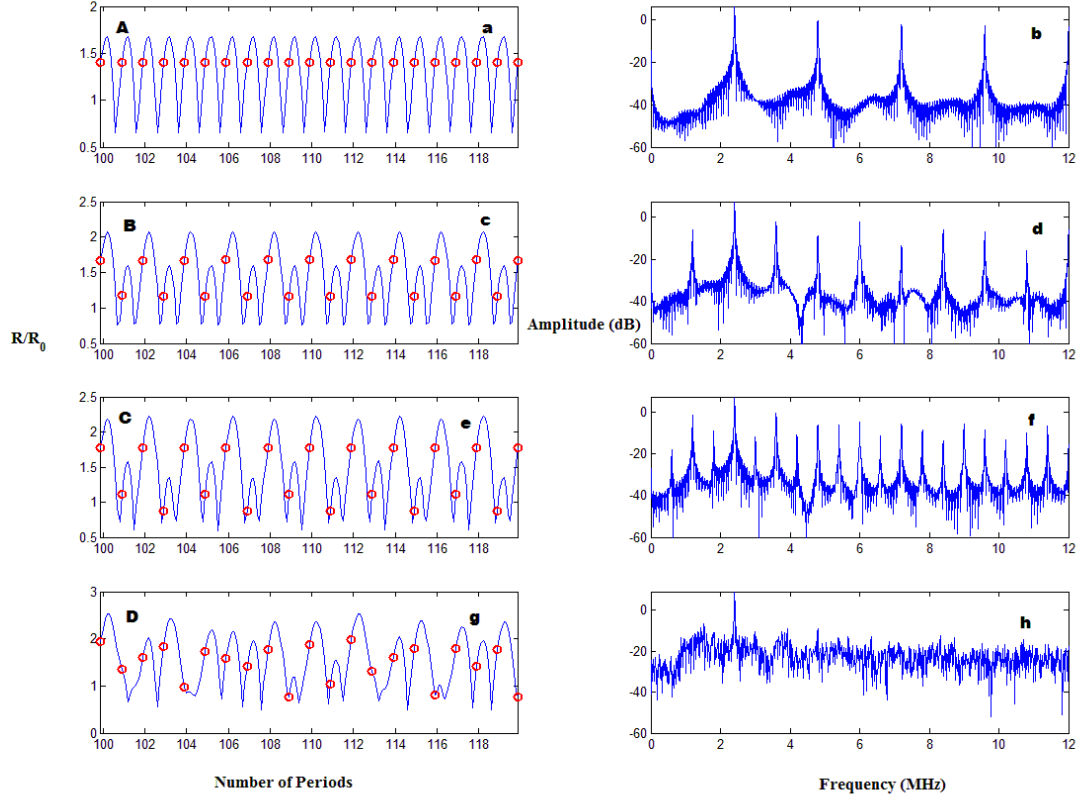
Figure 2.1: Left column: The normalized radial oscillations (R(t)/R0) versus the driving period of a 4 micron bubble with G_s=50 MPa, μ_s =0.7066 Pa.s, θ=3nm. The driving frequency is 2.4 MHz and the pressure amplitude is 200, 325,377 and 500 kPa from top to bottom. (Red circles represent the R(t)/R$_0$ at the end of each acoustic driving period) Right column: the spectrum of the backscattered pressure (sampling frequency is 24 MHz).

The corresponding frequency domain response, as depicted in Fig. 2.1(b), shows that only frequencies that are integer multiples of the fundamental frequency (f = 2.4 MHz) are present in the bubble behaviour. By increasing the transmit pressure amplitude to 325 kPa (Fig. 2.1(c)), results in a period-2 oscillation. In this case the bubble repeats the same oscillatory response once in every two driving periods (after every 2T seconds). As shown in Fig. 2.1(d), the

frequency domain response contains frequencies of (m*f/2) MHz, m = 1, 2, 3, . . . A period 4 response is illustrated in Fig. 2.1(e) at the transmit pressure of 377 kPa. In this case the oscillatory pattern repeats itself after every four driving periods. Figure 2.1(f) shows that the frequency response contain of frequencies at m*f/4 MHz where m= 1, 2, 3, . . .,. by increasing the transmit pressure amplitude to 500 kPa (Fig. 2.1(g)), the radial oscillations of the bubble becomes chaotic. Chaotic oscillations correspond to a broadband frequency spectrum. The frequency domain response is shown in Fig. 1(h). The route to chaos has been demonstrated to correspond to harmonic, subharmonic, and ultraharmonic frequencies (Leighton et al. 1997), which is observable in the bubble response.

2.2.4 Construction of the Bifurcation diagram

The radial oscillatory behaviour shown in Fig. 2.1 can be represented in what is referred to as a "pressure-bifurcation" (Macdonald & Gomatam 2006) diagram as shown in Fig. 2.2. It is calculated by selecting a starting transmit pressure of interest (50 kPa in this example) and then solving equations (1) and (2). Afterwards the value of the radial oscillations (R(t)) will be calculated at the end of each driving period and between a specific range (80T and 100T in this example). This will result in 20 values (in this example as the range consists of 20T) and these values will be plotted as a function of the pressure amplitude in the bifurcation diagram. These values (between 80T and 100T) were chosen to make sure that the analysis of the bifurcation points in last 20 cycles are carried out in the stable regime of oscillations while the initial transient oscillations have been decayed. Also 20 cycles will enable us to be able capture period 2, 3, 4, 5 and chaotic oscillations. As an example in period 4 oscillations the bubble repeats the same behaviour every 5 acoustic cycles and therefore having a 20 period range for the analysis

ensures that the bubble will have repeated the oscillatory pattern for 4 cycles, and therefore the dynamics can be captured in this analysis. The pressure amplitude is then increased by a small amount (1 kPa) and the same procedure is carried out in small pressure increments up to a transmit pressure value of interest (500 kPa in Figure 2.2). Looking at Fig. 2.1(a), only one point is seen at 100 kPa on the bifurcation diagram. This is because all the 20 values of R(t) are plotted on each other which represents a period 1 oscillation. Looking at Fig. 2.1(b), two points are seen on the bifurcation diagram. The bubble exhibits period 2 oscillations, for any transmit pressure value in region B of Fig. 2.2. Looking at Fig. 2.1(e), four points are visible on the bifurcation diagram corresponding to the transmit pressure value of 377 kPa. The bubble exhibits period 4 oscillations for the pressure values in the region C in Fig. 2.2. By increasing the driving pressure amplitude to ~400 kPa the system oscillatory response becomes chaotic. In this case up to 20 points are plotted at each transmit pressure amplitude value. It should be noted that, the bubble response is not chaotic for all of the values of the transmit pressure above 400 kPa. At around 450 kPa, there is a very small window of regular behaviour. As seen a small change in the acoustic pressure (Pa) can result in a regular or chaotic behaviour.

In our analysis, the bifurcation diagram was also used to plot the amplitude of the subharmonics in the backscattered signal as a function of incident pressure. For example, the bifurcation diagram for the subharmonic of order 2/3 was done as follows: the backscattered pressure was calculated for 30 cycles of sonication. Then the frequency spectrum was calculated. In the frequency spectrum the amplitude corresponding to the frequency of 2/3 the driving frequency was found and was plotted versus the corresponding driving pressure. Then the pressure was increased by an small increment and the amplitude of the 2/3 was found and plotted

versus the new pressure. The approach was repeated until the whole pressure range of interest was covered.
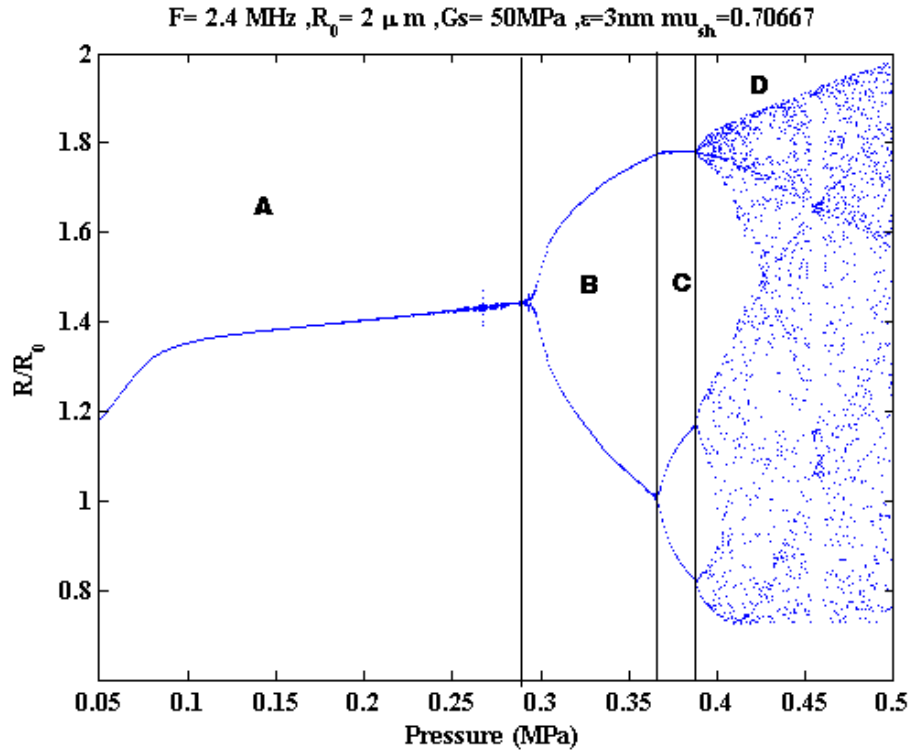
Figure 2.2: Bifurcation diagram of the normalized radial oscillations (R(t)/R0) versus the driving pressure of a 4 micron diameter bubble with G_s=50 MPa, μ_s =0.7066 Pa.s,Θ=3nm. The driving frequency is 2.4 MHz .

2.2.5 Ring down analysis for bubble sizing

The results obtained by numerical simulation of the Hoff model are based on single bubble backscattering. The predicted bubble oscillations are highly sensitive to exposures at frequencies close to the resonant frequency of the bubble and the resonance frequency of the bubbles is size dependent. However the experiments performed (described later in 2.3.1-2.3.3) were based on sonicating a polydisperse population of the bubbles with different resonance frequencies. The

experimental results showed that sub-population of bubbles were able to generate the predicted model behavior. Since the size distribution was polydisperse and the resonance frequencies of the bubbles were not known, directly relating the theoretical predictions with experimental data was impossible. A method was developed to analyze the signals obtained by sonicating a polydisperse population of bubbles, isolating the signal from a signal bubble of unknown size, and estimating its' resonance frequency. In this method the free damped oscillations of the bubble after the driving acoustic force is turned off was analyzed. The frequency of the free oscillations is approximately equal to the original resonance frequency of the bubble.

To illustrate the concept described above, simulation results are presented. After the acoustic driving force is off, the bubble still continues to oscillate for a small number of cycles. The free oscillations after the sonication are called ring-down oscillations. The length of the ring-down oscillations depends on the viscosity of the shell and the medium surrounding the bubble. More viscous shells or more viscous mediums induce a larger damping; therefore the bubble ring down dampens sooner in time. Figure 2.3a-d shows the oscillations, backscatter, frequency content and the ring-down frequency, respectively, of a bubble due to a 60 cycle long acoustic insonation at 25 MHz. After turning off the acoustic force the bubble oscillates for 3-4 cycles. Frequency analysis of the backscattered pressure confined to the ring-down oscillations shows that the frequency of free oscillations is equal to the resonance frequency of the bubble. In our experiments the frequency content of the ring-down oscillations were used to estimate the resonance frequency of the given bubble, which is further described in the experimental methods. This method has also been used to estimate the resonance frequency of a lipid shell microbubble using high speed optical camera with a temporal resolution of 10 ns (Sun et al. 2005).
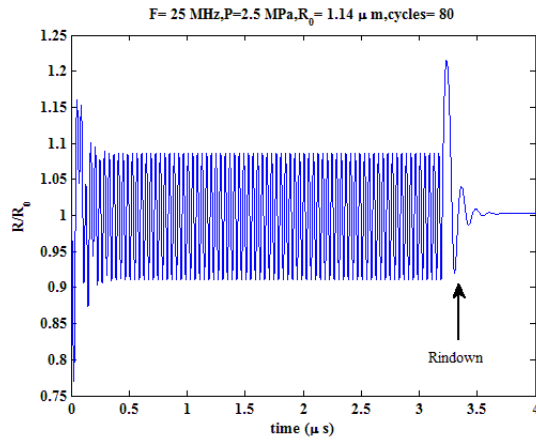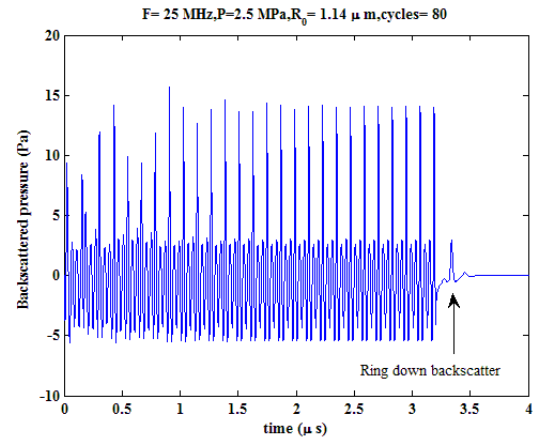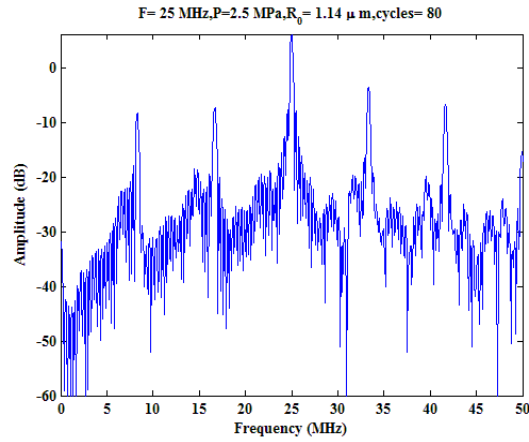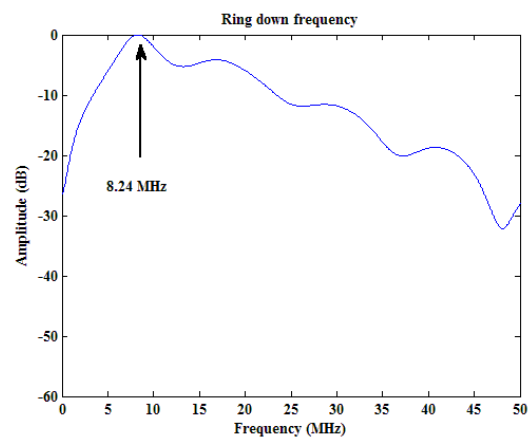
Figure 2.3: a) Radial oscillations, b) Backscattered pressure, c) frequency spectrum of the backscattered pressure and d) frequency spectrum of the ring-down oscillations only for a 2.28 micron bubble driven at 25 MHz and 2.5 MPa of pressure. Comparison of the power spectra (c) and (d) illustrate that during the ring-down, the microbubble oscillates at its resonant frequency.

2.3.1 Experimental methods

Ultrasonic data acquisition was performed using a VEVO770 ultrasound imaging device (VisualSonics Inc. Toronto, Ontario). Radiofrequency data were collected at a sampling rate of 420 MHz. A broadband focused Polyvinylidene Fluoride transducer (the RMV-710B), with a resonance frequency of 25 MHz, f-number of 2.1, focal length of 15 mm, and -6 dB bandwidth of 12-28 MHz was employed. Applying a 10 kHz pulse repetition frequency, 100 ultrasonic raw RF lines spaced 0.1586 mm apart were acquired from different lateral positions of a 2.64 mm*15.86 mm RF window for each ultrasound frame. Two different types of bubbles were used in these experiments. The microbubbles were allowed to float in dilute suspensions in deionized water, so that when the imaging was done signals from individual microbubbles would be easily differentiated. Figure 2.4 shows such a signal from a single bubble as shown on the console of the imaging device. The solutions used were very dilute thus the bubble-bubble interaction is minimal. On the other hand the chosen RF line includes just one bubble (bottom left window). The resulting signal is shown on the bottom right window in red and the corresponding power spectrum is in blue.

Despite the fact that care has been taken to isolate the signals from single bubbles and reduce the interaction between bubbles, sometimes interaction between bubbles were inevitable, or isolating a single signal was impossible. Therefore such signals were excluded from analysis. Figure 2.5 shows an inappropriate signal for analysis. Further information on the procedure for isolating single scatterers from dilute solutions can be found elsewhere (Falou et al. 2008).
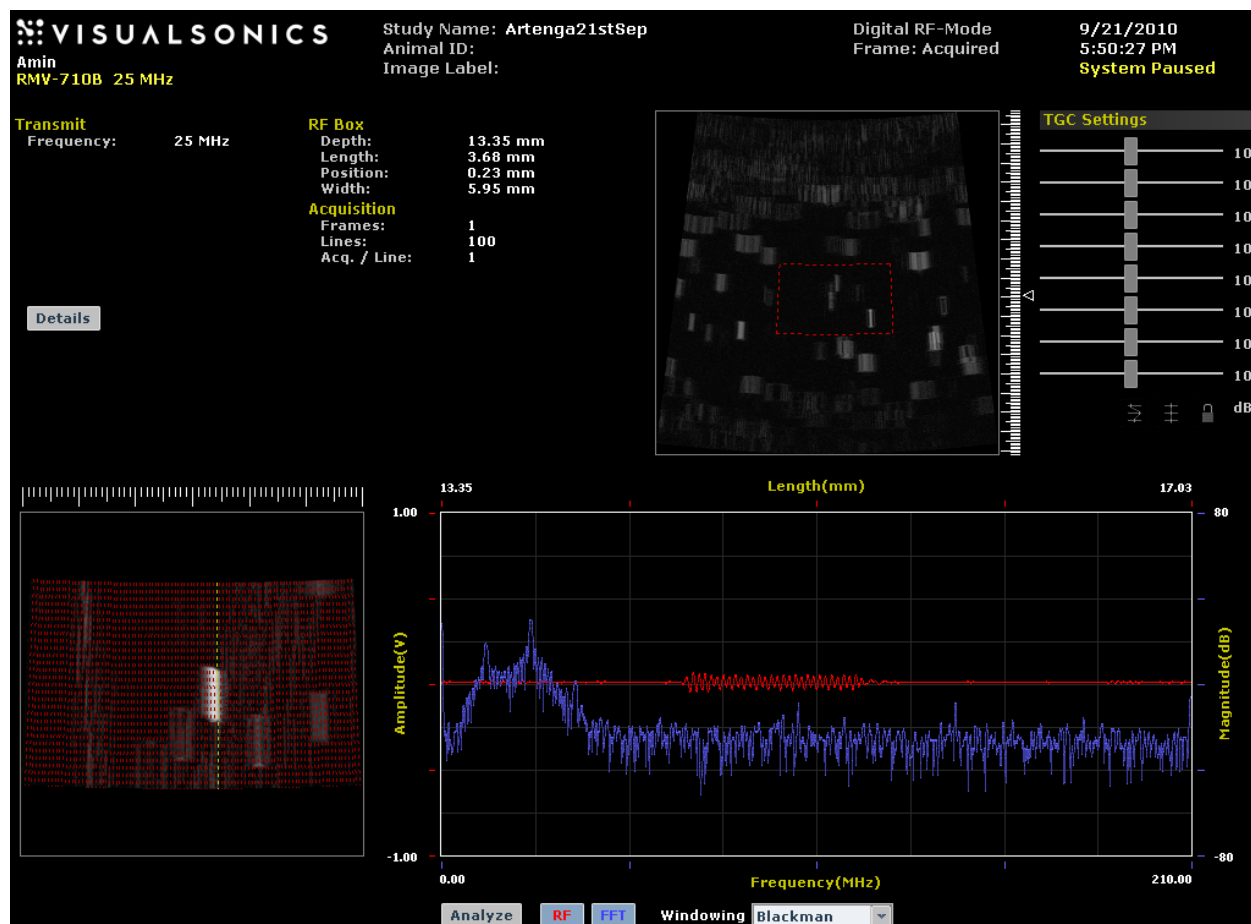
Figure 2.4: The signal from single Artenga bubble sonicated with frequency of 25 MHz and 10% of power.
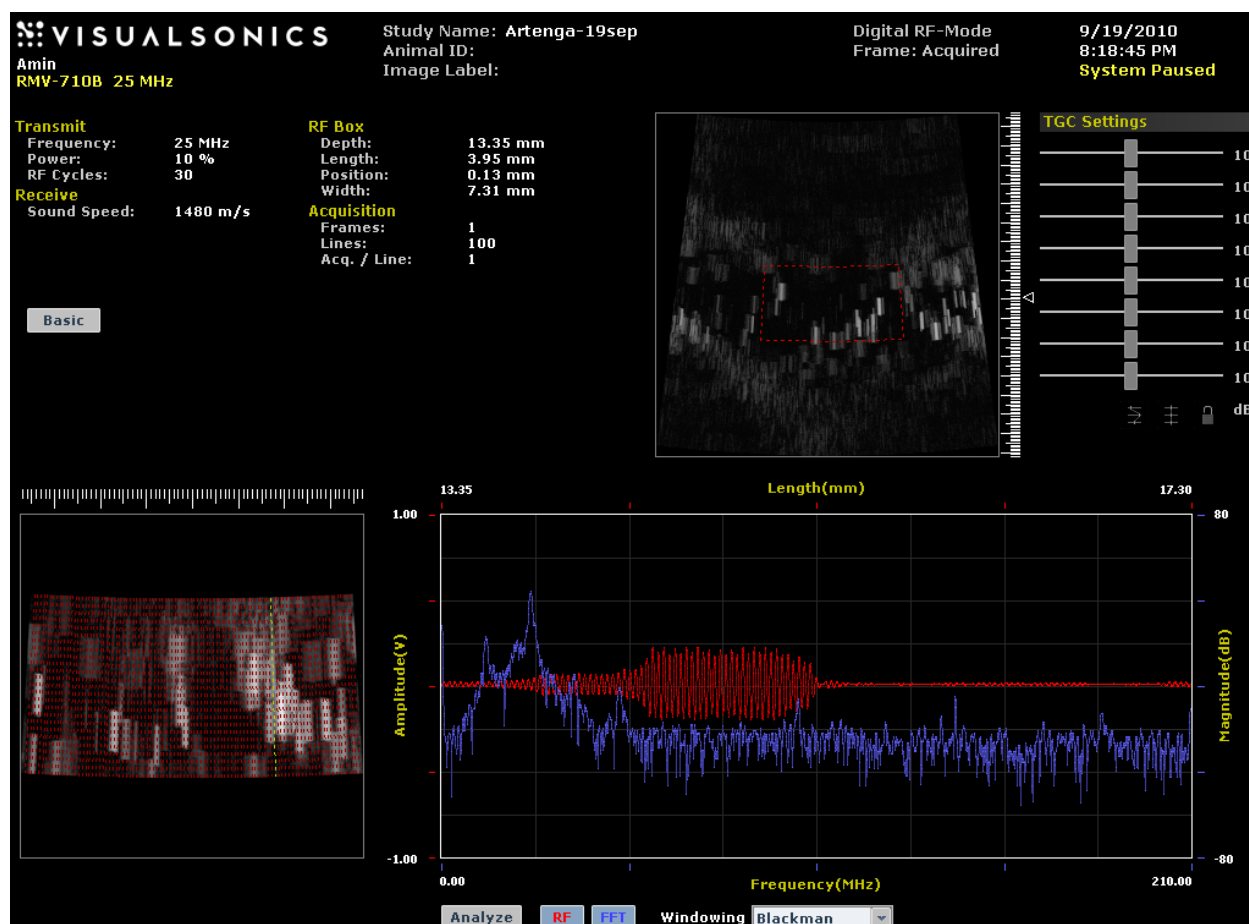
Figure 2.5: Inseparable signal from single Artenga bubbles. The sonication frequency is 25 MHz with 10% power.

2.3.2 Experiment with in-house made lipid coated bubbles

A microfluidic device manufactured from polydimethylsioxane (PDMS) (Gong et al. 2010) was employed and mixed a lipid solution and octafluoropropane that were pushed through the liquid and gas channels of the device. In the flow focusing chamber, the central stream of gas and two lateral streams of liquid merged and are forced through a 7-μm orifice. Microbubbles pinch off on the opposite side of the orifice, and by maintaining the liquid flow rate and gas pressure constant it was possible to produce microbubbles with very narrow size distributions.

Bubbles with very narrow size distributions of 3, 4.6, 6.2 and 6.6 μm were sonicated with pulses that had peak pressures ranging between 75 kPa-2.5 MPa and that consisted of 3-30 cycles. The signals belonging to 30 cycles of insonation were chosen to be analyzed as longer pulses produce better seperation between the frequency components of the received signals. This makes the comparison with the numerical methods easier. In all cases the transducer was placed so that the focal point of the transducer was at least 2 cm away from the bottom of the glass container that the solution was housed in. For each case the experiments were repeated at least 5 times and each time 100 radio frequency signal was obtained to be analyzed later.

2.3.3 Experiment with Artenga bubbles

A 2 μl volume of Artenga bubbles were injected to a cylindrical custom made plexiglass container filled with distilled water. This concentration was chosen so that to decreases the interaction between the bubbles as much as possible. The diameter and height of the container was 5 cm and it was filled with approximately 78.5 ml of deionized water. The insonations were done with 30 cycle sinusoidal pulses of 1.25 MPa and 2.5 MPa amplitude. In all cases the transducer was placed so that the focal point of the transducer was at least 2 cm far away from the bottom of the glass container. The experiments were repeated for at least 20 times for each pressure amplitude and each time 100 radio frequency signals were obtained to be analyzed later.

2.3.4 Signal Analysis

Visual inspection was performed on the stored signals to separate the signals of the single bubbles from the signals which were not distinguishable from each other. The same methodology used to isolate signals from single cells is described elsewhere (Falou et al. 2008). The

frequency content of the chosen signals were then analyzed using the MATLAB 7 package (The MathWorks, Inc., Natick, MA). As only the signals from the single bubble scattering were considered, the RF signal contained only the signal from the bubble. Therefore the frequency analysis was performed over the full window of the extracted RF signal.

In order to perform the ring down analysis a further set of qualification criteria were applied. The criteria were a) that the free oscillations at the end of the signals should be differentiable from the noise floor and b) that there was enough separation between the end of the ring-down of the signal and the next subsequent signal of the RF line (if present), so that the free oscillations at the end of the signal of interest are easily differentiable from the presence of any subsequent signal. This ensures that the analysis is limited to signals produced by the ring-down of the oscillating bubble.

Chapter 3 Results

3.1 Theoretical results

The Hoff model (equation 1) was solved and the bifurcation diagrams of the normalized oscillations of the bubble were calculated. The results enabled us to define a new classification scheme for the bubble oscillations in terms of its resonance frequency. The dynamics of a sample case are first presented (R_0=0.8789 µm, G_s=108MPa, shell thickness=3 nm, μ_{sh}= 0.062 Pa.s). The natural resonance frequency of this bubble is 12.5 MHz. The shell parameter values are calculated based on the reported values at high frequencies for Definity (Goertz et al. 2007). The simulation results is repeatable for every bubble with different shell parameters as long as the resonance condition, the insonation frequency and the threshold pressure are chosen correctly and in accordance to the classification scheme defined later in section 4.

Figure 3.1 shows the bifurcation structure of the bubble when it is sonicated at 25 MHz (twice its natural resonance frequency). The bubble exhibits linear period one oscillations for lower driving pressures and as soon as the pressure increase is above ~500 kPa the radial oscillations undergo a period doubling bifurcation and the bubble begins exhibiting a subharmonic response. The bubble will sustain this behaviour for a wide range of applied pressures before it undergoes further period doubling bifurcations which results in chaotic oscillations around 2 MPa. Figure 3.2 shows the subharmonic amplitude of the backscattered pressure versus the driving pressure for a 30 cycle insonation. The initiation of the subharmonics

is concomitant with the period doubling that occurs at the bifurcation (both begin around 450 kPa). There is a drop in subharmonic amplitude as the higher periods appear in the bubble behaviour and therefore this feature is not suitable for imaging. In this case, the subharmonic amplitude versus pressure was not considered for driving pressures more than 2 MPa because the bubble passes the destruction threshold (R0/R>2) (Flynn & Church 1988). The occurrence of the chaotic oscillations may decrease the subharmonic amplitude as the energy of the signal is now divided over a very large frequency range. In order to better analyze the bubble dynamics one can consider the radial oscillations versus time, the corresponding backscattered signal and its frequency content. These are shown respectively in Figures 3.3a-c. The backscattered pressure has two maxima and there is a ring-down component at the end of the signal. The frequency spectrum of the backscatter clearly shows a significant subharmonic at 12.5 MHz.

Figure 3.1: Bifurcation diagram of the normalized radial oscillations (R/R0) versus the driving pressure of a 1.76 µm bubble with G_s=108 MPa, μ_s =0.062 Pa.s,Θ=3nm. The driving frequency is 25 MHz at the length of the pulse is 30 cycles.

Figure 3.2: Half order subharmonic amplitude (1/2) versus the driving pressure of a 1.76 μm bubble with G_s=108 MPa, μ_s =0.062 Pa.s,Θ=3nm. The driving frequency is 25 MHz.
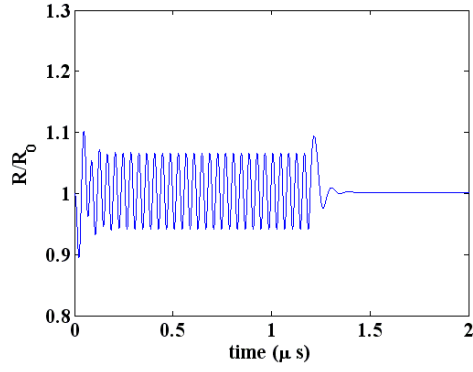
(a)
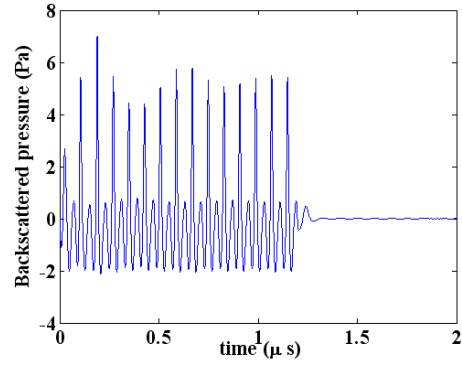
(b)
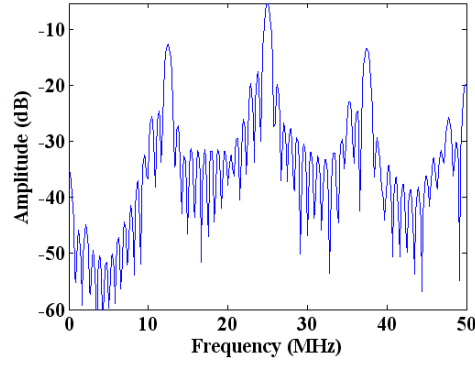
(c)

Figure 3.3: a) Radial oscillations (R(t)/R0) versus time of a 1.76 µm bubble with G_s=108 MPa, μ_s =0.062 Pa.s,Θ=3nm. The driving frequency is 25 MHz, the length of the pulse is 30 cycles and the pressure amplitude is 1 MPa , b) the corresponding backscattered pressure, c) the frequency spectrum of the backscattered pressure.

Figure 3.4 shows the bifurcation structure of the bubble versus pressure when the driving frequency is 36 MHz which is slightly less than three times its resonance frequency (37.5 MHz). The bubble exhibits linear oscillations for pressure less than 2 MPa. As soon as the pressure increases above 2 MPa there is a saddle node bifurcation to period three oscillations. The bubble sustains this behaviour until the driving pressure is increased above 3 MPa. Figure 3.5 shows the amplitude of the 2/3 subharmonic in the backscattered pressure versus the driving pressure. The subharmonic amplitude at 24 MHz undergoes a sudden increase concomitant with the occurrence of period three oscillations in the bifurcation structure. Afterwards, the 2/3 subharmonic amplitude gradually increases and plateaus before a significant drop concomitant with the reduction of period three oscillations.

The results of the analysis of the radial oscillations, the corresponding backscattered pressure and its frequency content at a pressure of 2.5 MPa are shown in Figures 3.6a-c respectively. The ring-down oscillations are clearly seen at the signal end. The backscattered pressure has three maxima and its frequency content has significant subharmonics at 12 MHz, 24 and ultraharmonics at 48 and 60 MHz.
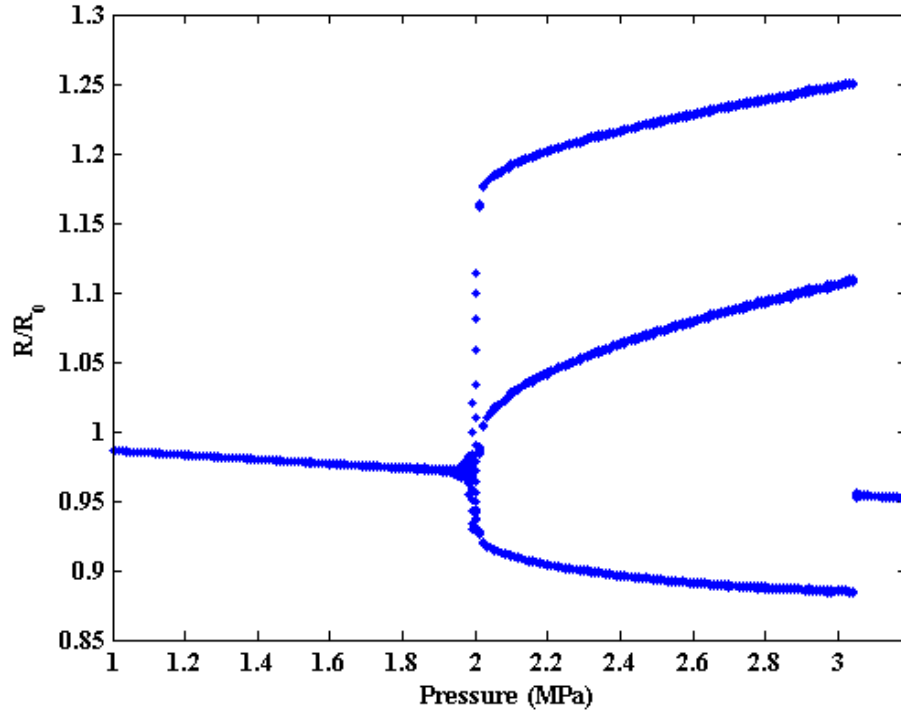
Figure 3.4: Bifurcation diagram of the normalized radial oscillations (R/R0) versus the driving pressure of a 1.76 µm bubble with G_s=108 MPa, μ_s =0.062 Pa.s,Θ=3nm. The driving frequency is 36 MHz and the pulse length 30 cycles.
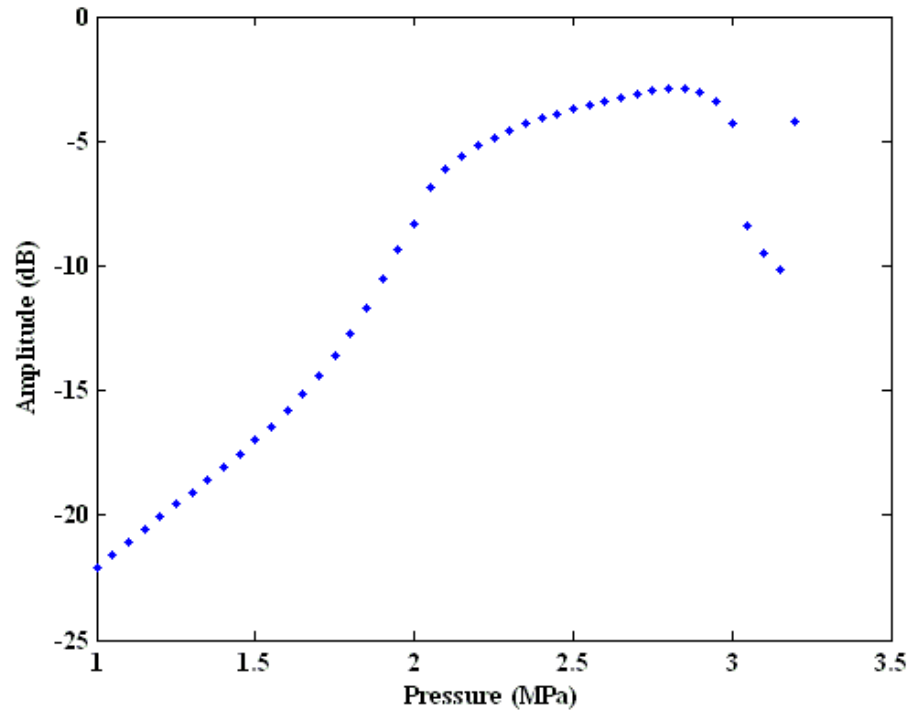
Figure 3.5: 2/3 order subharmonic amplitude (24MHz) versus the driving pressure of a 1.76 µm bubble with G_s=108 MPa, μ_s =0.062 Pa.s,$\ominus$=3nm. The driving frequency is 36 MHz and the pulse length 30 cycles.

(a)

(b)

(c)
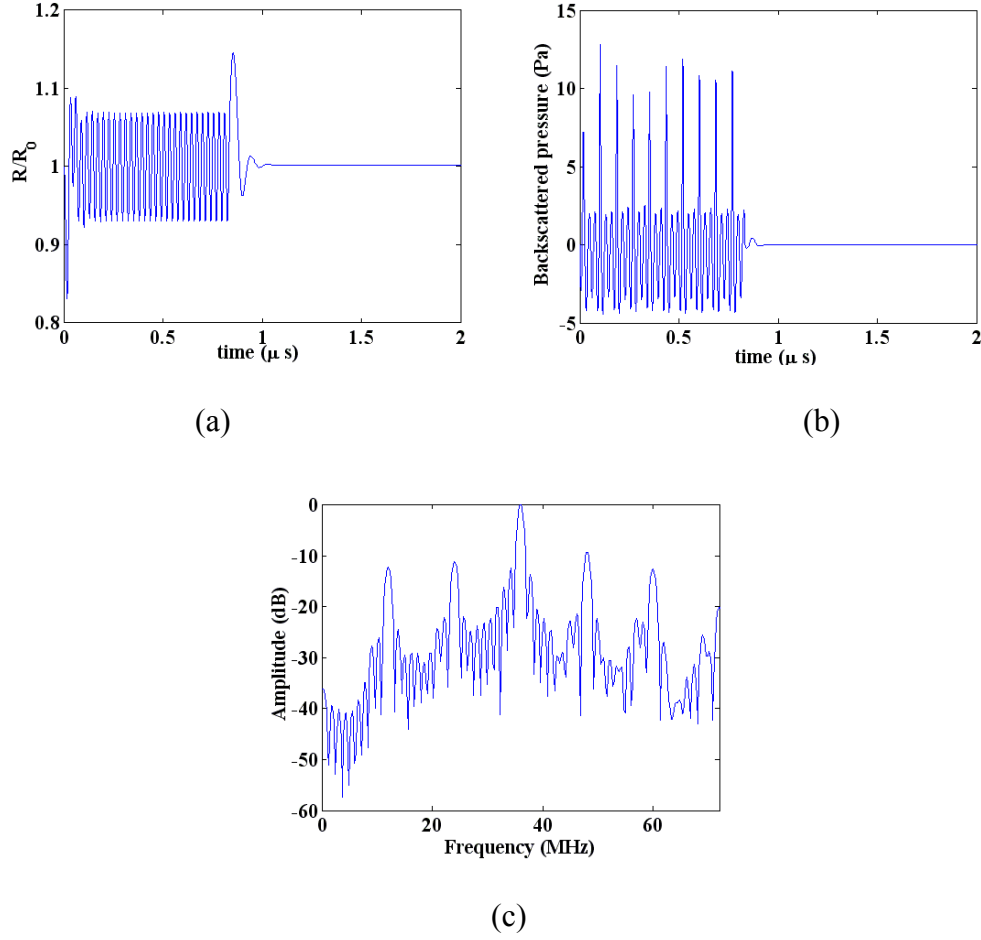
Figure 3.6: a) Radial oscillations (R(t)/R0) versus time of a 1.76 μm bubble with G_s=108 MPa, μ_s =0.062 Pa.s,Ɵ=3nm. The driving frequency is 36 MHz, pulse length 30 cycles and the pressure amplitude is 1 MPa, b) Corresponding backscattered pressure, c) frequency spectrum of the backscattered pressure

Figure 3.7 shows the bifurcation structure of the normalized oscillations of the bubble versus pressure when the driving frequency is 46 MHz which is slightly less than 4 times its resonance frequency (50MHz). The bubble behavior is linear for pressures less than the threshold pressure of ~4 MPa. After the driving pressure increases above 4 MPa the bubble oscillations undergo a saddle node bifurcation to period 4 oscillations. The bubble sustains this behavior for pressures up to ~4.7 MPa. Analysis of the ¾ subharmonic amplitude versus pressure in Figure 3.8 shows

42

that the 34.5 MHz subharmonic undergoes a sudden increase concomitant with the occurrence of period 4 oscillations. It reaches a saturation level and then suddenly decreases as the period four oscillations disappear.
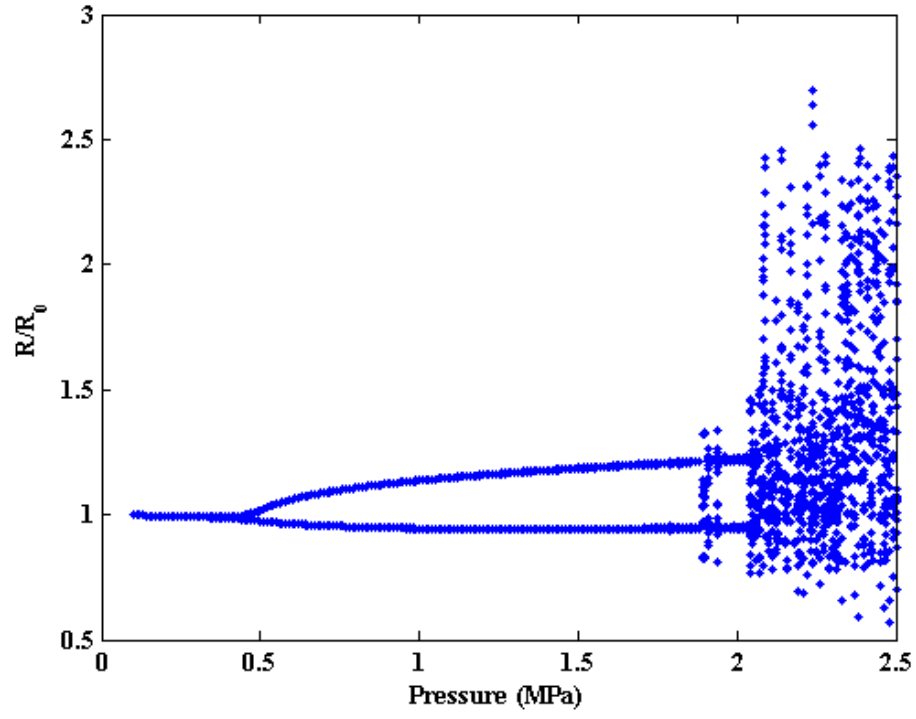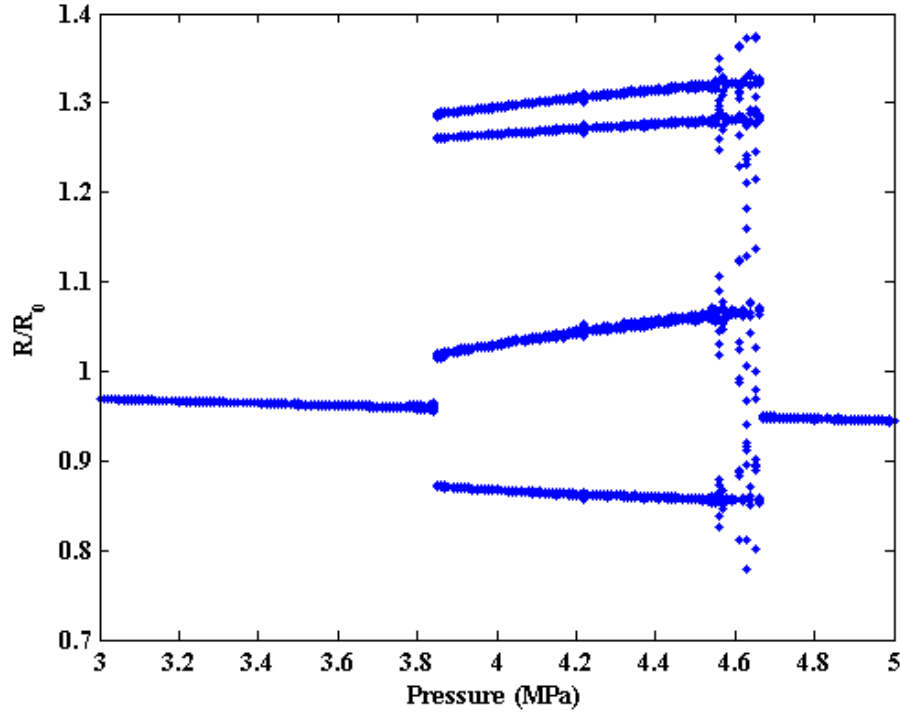

Figure 3.7: Bifurcation diagram of the normalized radial oscillations (R/R0) versus the driving pressure of a 1.76 micron bubble with G_s=108 MPa, μ_s =0.062 Pa.s, Θ=3nm. The driving frequency is 46 MHz and the incident pulse length 30 cycles.
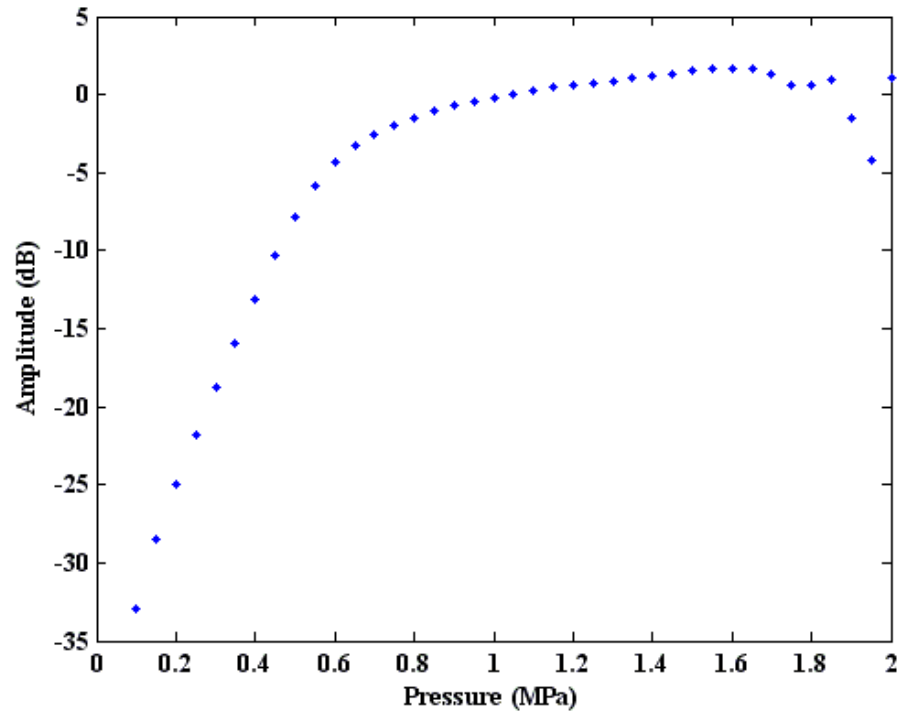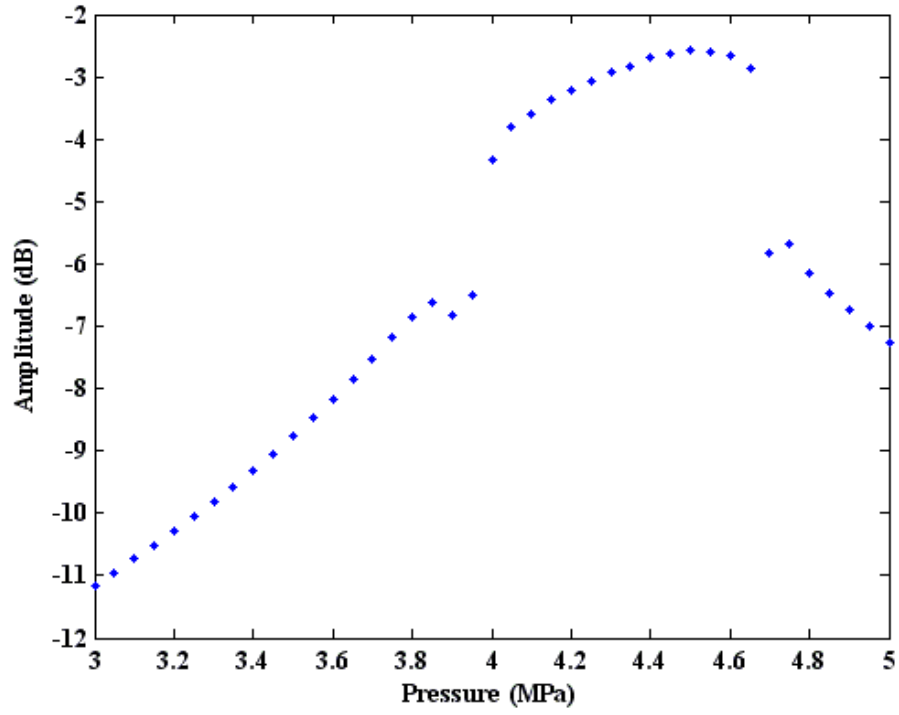
Figure 3.8: 3/4 order subharmonic amplitude versus the driving pressure of a 1.76 micron bubble with G_s=108 MPa, μ_s =0.062 Pa.s, Θ=3nm. The driving frequency is 46 MHz.

Figures 3.9a-c show the radial oscillations, the corresponding backscattered pressure and the power spectrum of the backscatter for a 4.2 MPa acoustic pressure. The backscattered pressure has 4 maxima and its frequency content has 3 subharmonics at 11.5, 23 and 34.5 MHz with ultraharmonics at 57.5, 69 and 80.5 MHz.

(a)   (b)

(c)
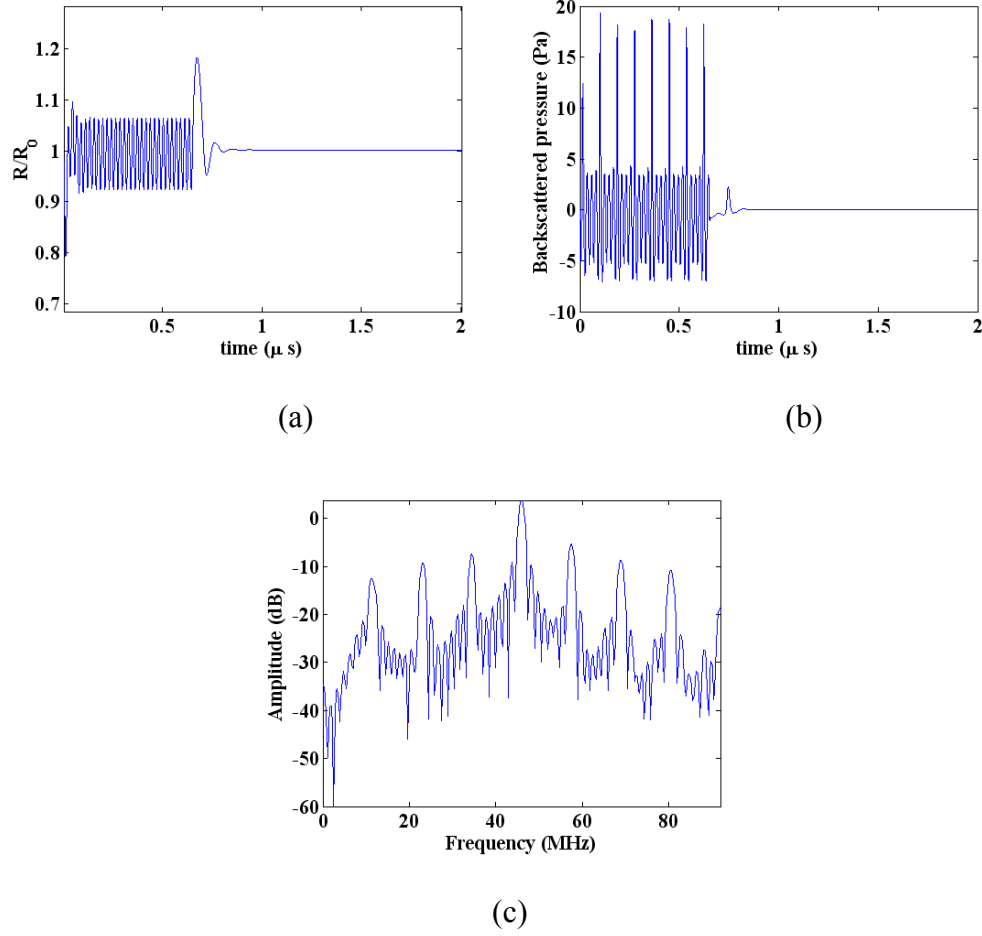
Figure 3.9: a) Radial oscillations (R(t)/R0) versus time of a 1.76 micron bubble with G_s=108 MPa, μ_s =0.062 Pa.s,Θ=3nm. The driving frequency is 46 MHz and the pressure amplitude is 4.2 MPa , b) Corresponding backscattered pressure, c) frequency spectrum of the backscattered pressure

Figure 3.10 shows the bifurcation structure of the normalized oscillations of the bubble versus pressure when the driving frequency is 55 MHz which is less than five times the resonance frequency of the bubble. Linear oscillations occur below a threshold pressure of ~ 6.2 MPa. The bubble sustains this behavior for pressures of approximately 6.8 MPa. The 4/5 subharmonic amplitude (44 MHz) versus the driving pressure is shown in Figure 3.11. As seen the subharmonic amplitude undergoes a rapid increase at a point of period 5. There is a saturation

45

region corresponding to the period five region in the bifurcation diagrams and then the drop region corresponding to the annihilation point of the 5 coexisting attractors (period 5 oscillations) at a pressure of approximately 6.8 MPa.
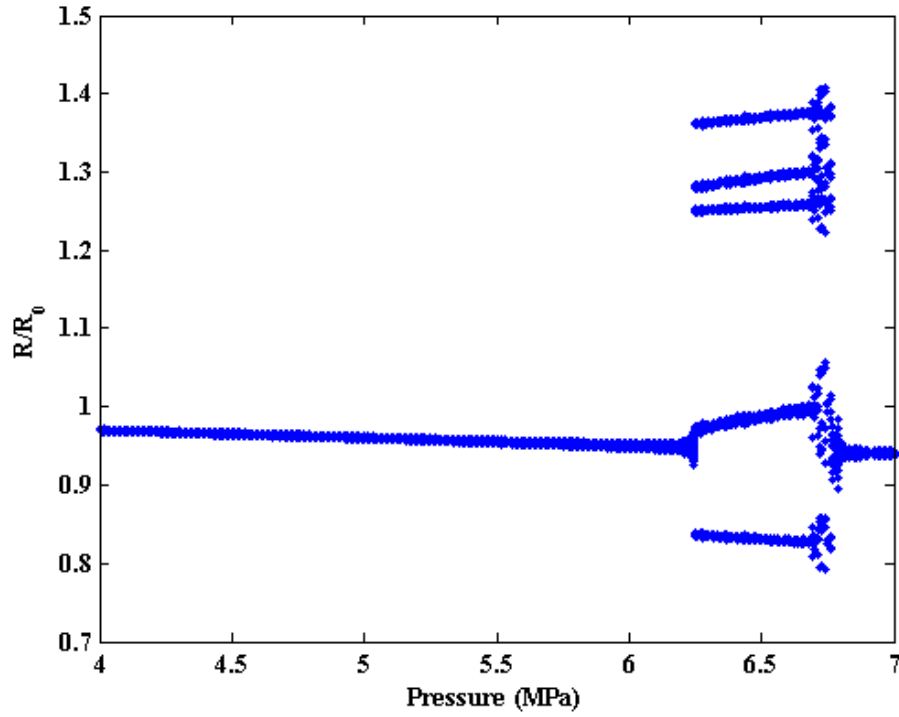
Figure 3.10: Bifurcation diagram of the normalized radial oscillations (R/R0) versus the driving pressure of a 1.76 µm bubble with G_s=108 MPa, μ_s =0.062 Pa.s,Θ=3nm. The driving frequency is 55 MHz.
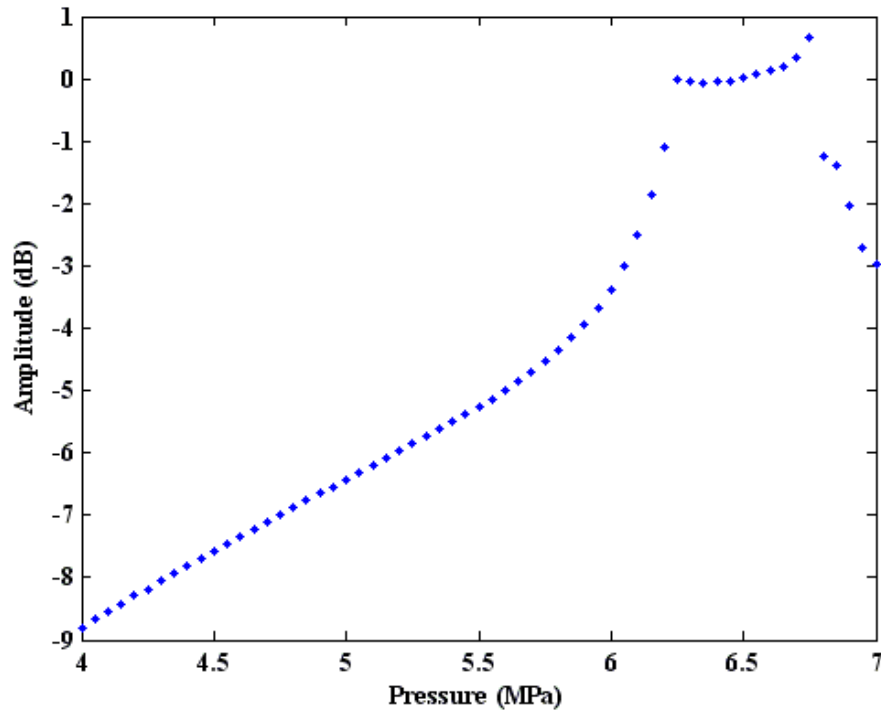
Figure 3.11: 4/5 order subharmonic amplitude versus the driving pressure of a 1.76 μm bubble with G_s=108 MPa, μ_s =0.062 Pa.s, $\ominus$=3nm. The driving frequency is 55 MHz.

Figures 3.12a-c shows the radial oscillation, backscattered pressure and it frequency content when the insonation pressure is 6 MPa at 55 MHz. The backscattered pressure has five maxima and its frequency spectrum has four subharmonics at 11, 22, 33 and 44 MHz with ultraharmonics at 66, 77, 88 and 99 MHz.

(a)   (b)

(c)
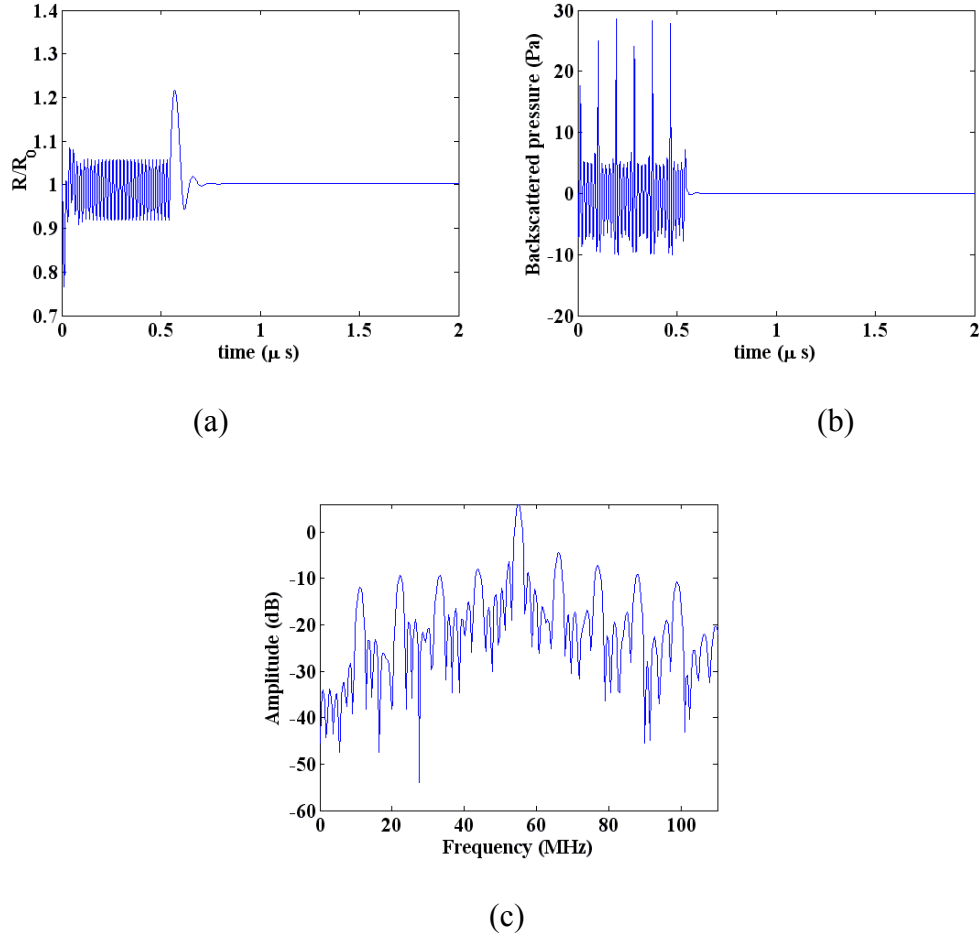
Figure 3.12: a) Radial oscillations (R(t)/R0) versus time of a 1.76 μm bubble with G_s=108 MPa, μ_s =0.062 Pa.s,Ɵ=3nm. The driving frequency is 55 MHz and the pressure amplitude is 6 MPa, b) Corresponding backscattered pressure, c) frequency spectrum of the backscattered pressure.

It should be noted that the cases of the frequencies which was chosen to show the behaviours depicted in the bifurcation diagrams were arbitrary. These frequencies were chosen because as the UCAs were able to sustain the higher order subharmonic emissions for a wider range of driving pressure.
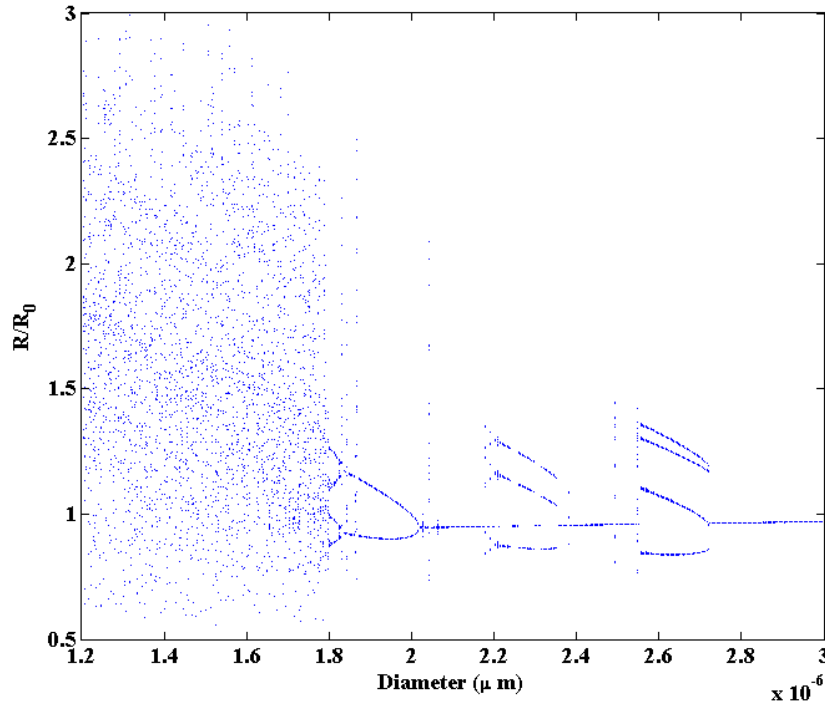
Figure 3.13: Bifurcation diagram of the normalized radial oscillations (R(t)/R0) versus the initial bubble diameter of a bubble with G_s=108 MPa, μ_s =0. 062 Pa.s, Θ=3nm. The driving frequency is 25 MHz and the pressure amplitude is 2.5 MPa.

The results shown are only based on sonicating a single size bubble. However in clinical practise the bubble size distribution is polydisperse. Because of this it is helpful to see the behavior of a large size distribution of the bubbles when the pressure and the frequency are fixed. The bifurcation diagram of the bubble versus the initial diameter of the bubble shows the size dependent behavior of the bubble together with their specific nonlinear response. Figure 3.13 shows the bifurcation diagram of the normalized oscillations of the bubble versus the bubble size for a frequency of 25 MHz and a pressure of 2.5 MPa. Smaller bubbles which are resonant at 25 MHz undergo chaotic oscillations and their normalized oscillation amplitude exceeds the destruction threshold (R/R0>2). Bubbles with diameters between 1.8-2 microns in

size are able to produce subharmonics at 12.5 MHz and their behaviour is characterized by period two oscillations. Slightly bigger bubbles between 2.2-2.4 micron are able to exhibit period three oscillations and subharmonics at 8.33 and 16.66 MHz. Bubbles with diameters between 2.5-2.7 micron exhibit period four oscillations and subharmonics at 6.25, 12.5 and 18.75 MHz. For a sufficient high pressure amplitude there exist subpopulation of bubbles in which their behaviour is characterized by period two, period three or higher period oscillations. The type of behaviour critically depends on the bubble size which determines its natural resonance frequency.

This prediction motivated the experimental part of this study which is based on insonation of a polydisperse bubble distribution at different pressure amplitudes. Signals from single bubbles satisfying the four different predicted behaviours illustrated above were isolated and were analyzed further to confirm the theoretical predictions.

3.2   Experimental results

Backscatter data were collected from two types of bubbles as described in section 2.2.2 and 2.2.3. In the first set of experiments, custom made lipid bubbles were examined, and in the second set of experiments, commercial Artenga bubbles were examined.

3.2.1 Signals from lipid bubbles

Custom made lipid bubbles (section 2.3.2) were sonicated with a 25 MHz pulse train with a pulse length of 30 cycles and at 100% power, corresponding to a peak pressure of ~ 2.5 MPa at the transducer focus (Iradji 2008). For further comparison with a signal from a linear reflector a layer of DC710 oil was also sonicated at the same acoustic settings. Figure 3.14 shows the

backscattered signal from DC710 oil as the linear reflector. The frequency of insonation is 25 MHz and the sonication is done at 50% of power with 30 cycles. As seen the response of the DC710 oil is linear and there is no subharmonic is present in the frequency spectrum. The backscattered signal also contains just one peak.
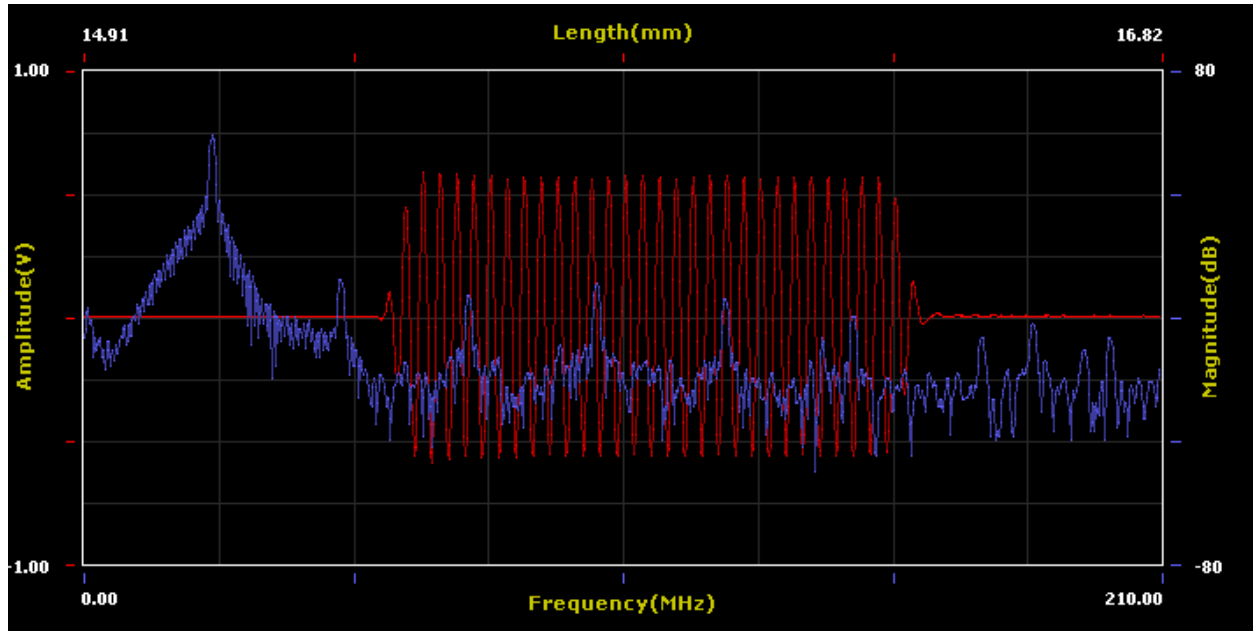
Figure 3.14:Measured backscattered signal (red) from insonating a linear reflector (DC710 oil) (red) and its frequency spectrum (blue). Transmit pulse have has a frequency of 25 MHz, pressure amplitude of 2.5 MPa and is 30 cycles long.

Figure 3.15 shows one of the measured backscatter signals from the lipid bubbles related to period 2 oscillations as a screen capture from the VEVO 770 console. The backscatter signal recorded is shown in red, while the blue color shows the frequency content of the signal (the power spectrum of the backscatter signal, without any filtering). The backscattered signal has two periods (two maxima) and the frequency response contains a significant subharmonic at 12.5 MHz. This is consistent with the theoretical predictions using the period-doubling bifurcation diagrams (Figure 3.1) and the subsequent backscattered pressure analysis.

51
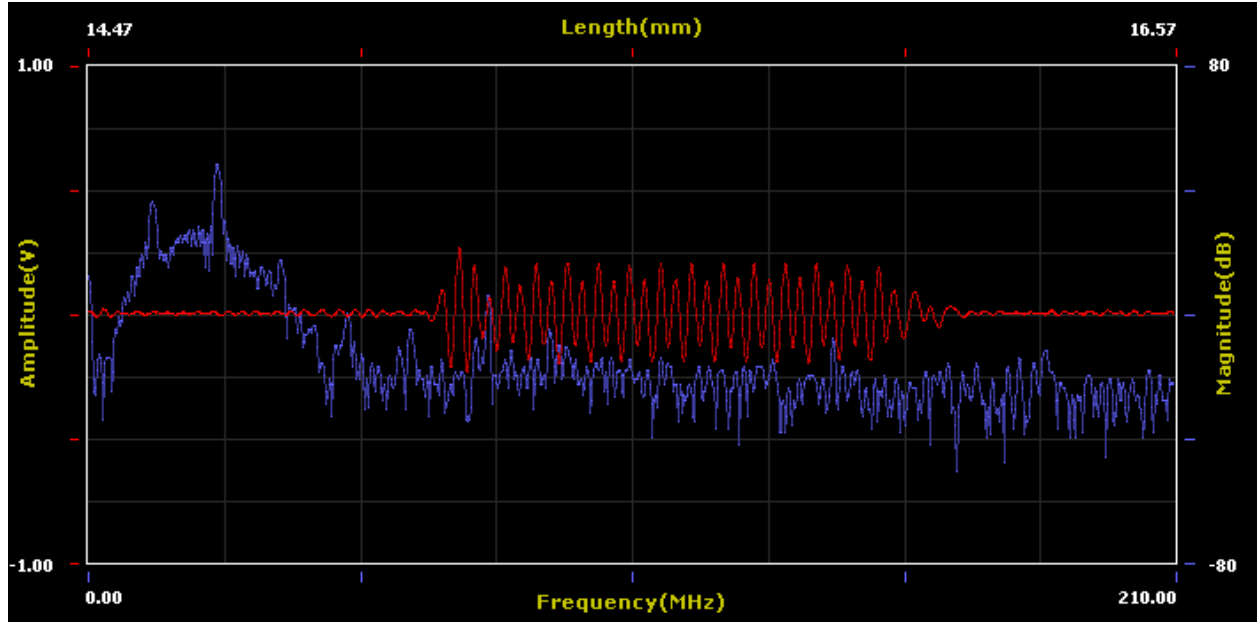
Figure 3.15: Measured period two backscattered signal (red) from insonating a lipid coated bubble and its frequency spectrum (blue). Transmit pulse has a frequency of 25 MHz, pressure amplitude of 2.5 MPa and is 30 cycles long.

Figure 3.16, illustrates the measurement of the period 3 backscatter signals. The backscattered pressure (red signal) has three maxima. The corresponding power spectra (blue) show the two subharmonics at 8.33 and 16.66 MHz. An ultraharmonic is also observable at 33.33 MHz, consistent with theoretical predictions.
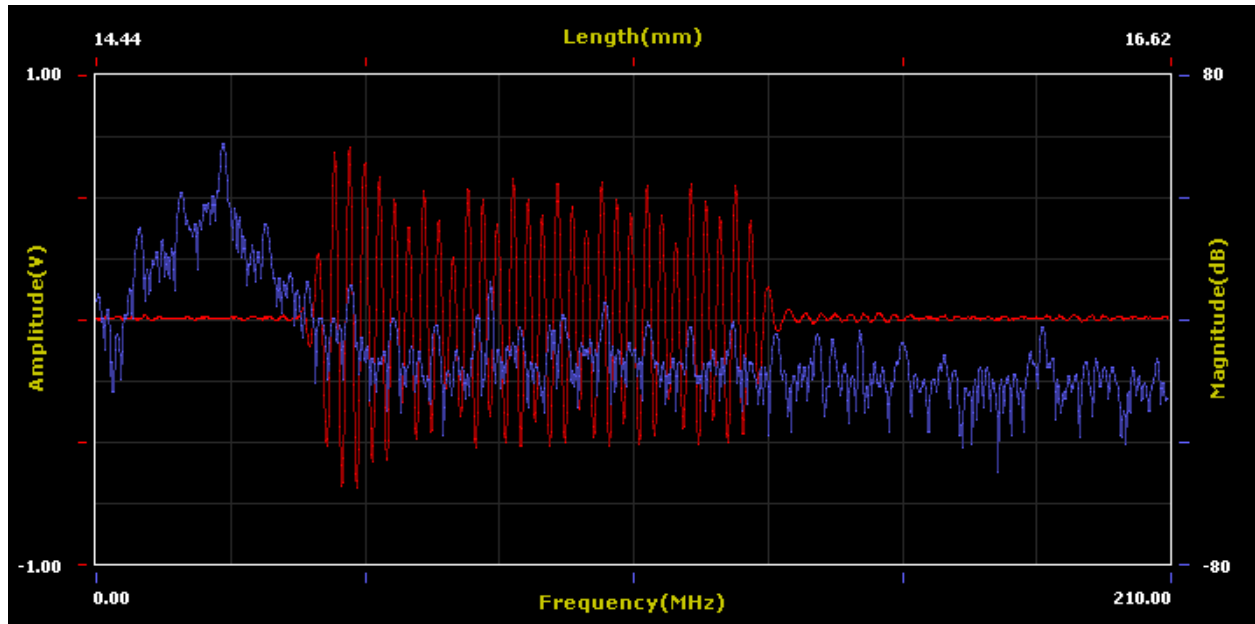
Figure 3.16: Measured period three backscattered signal (red) from insonating a lipid coated bubble and its power spectrum (blue). The transmit pulse has a frequency of 25 MHz, pressure amplitude of 2.5 MPa and is 30 cycle long.

3.2.2 Signals from Artenga bubbles

Artenga bubbles (section 2.2.2) were sonicated with a 25 MHz pulse train with a pulse length of 30 cycles and at 50% power, corresponding to a peak pressure of ~ 1.25 MPa at the transducer focus (Iradji 2008).

Figure 3.17 shows the backscatter signal from a period two oscillation in red and the corresponding frequency content (power spectrum) in blue. In addition to the major fundamental component of the signal at 25 MHz, a strong subharmonic at 12.5 MHz and a strong ultraharmonic at 37.5 MHz are noticeable.

Figure 3.18 depicts one of the measured period 3 backscatter signals. The red signal which shows the backscattered pressure consists of 3 maxima and the corresponding power spectrum (blue) shows 2 subharmonics at 8.33 and 16.66 and an ultraharmonic at 33.33 MHz.
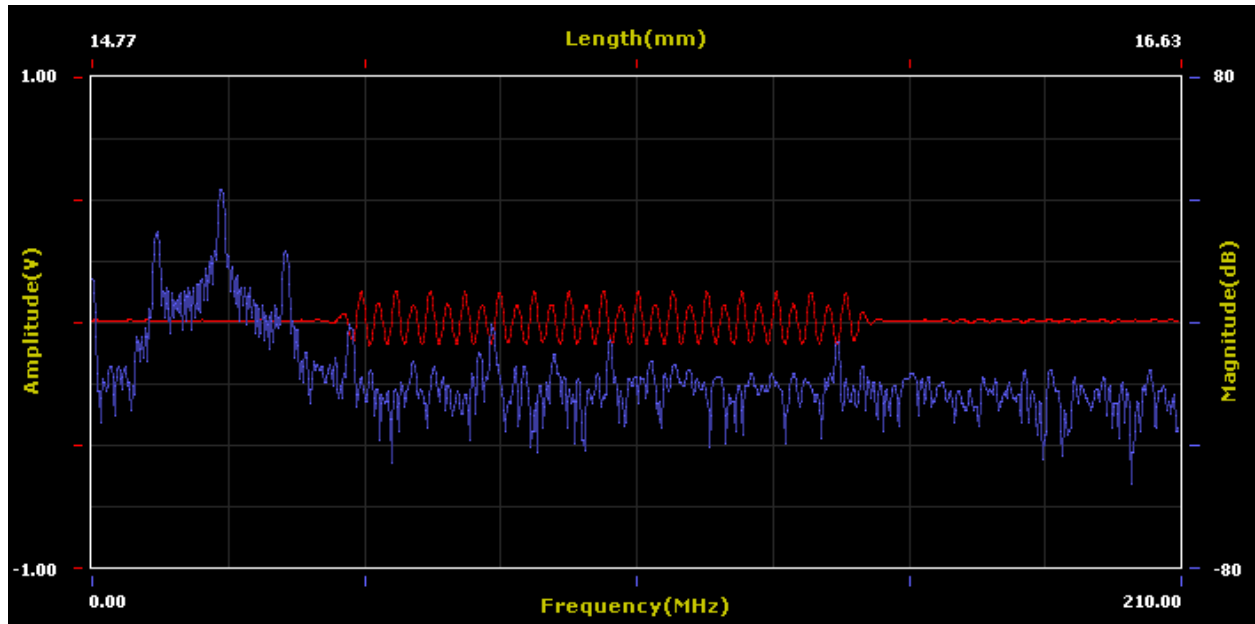
Figure 3.17: Measured period two backscattered signal (red) from insonating an Artenga bubble and its power spectrum (blue). The transmit pulse has a frequency of 25 MHz, pressure amplitude of 1.25 MPa and is 30 cycles long.

Figure 3.19 shows one of the measured period 4 backscatter signals. Four maxima are observed in the received signal. The power spectrum of the signal illustrates 3 subharmonics at 6.25 MHz, 12.5 MHz, 18.75 MHz and an ultraharmonic at 31.25 MHz. Figure 3.20 illustrates one of the measured period 5 backscatter signals. The detected backscattered signal has 5 maxima. In addition to the main fundamental frequency at 25 MHz, the signal has 4 subharmonics at 5, 10, 15 and 20 MHz and a strong ultraharmonic at 30 MHz.
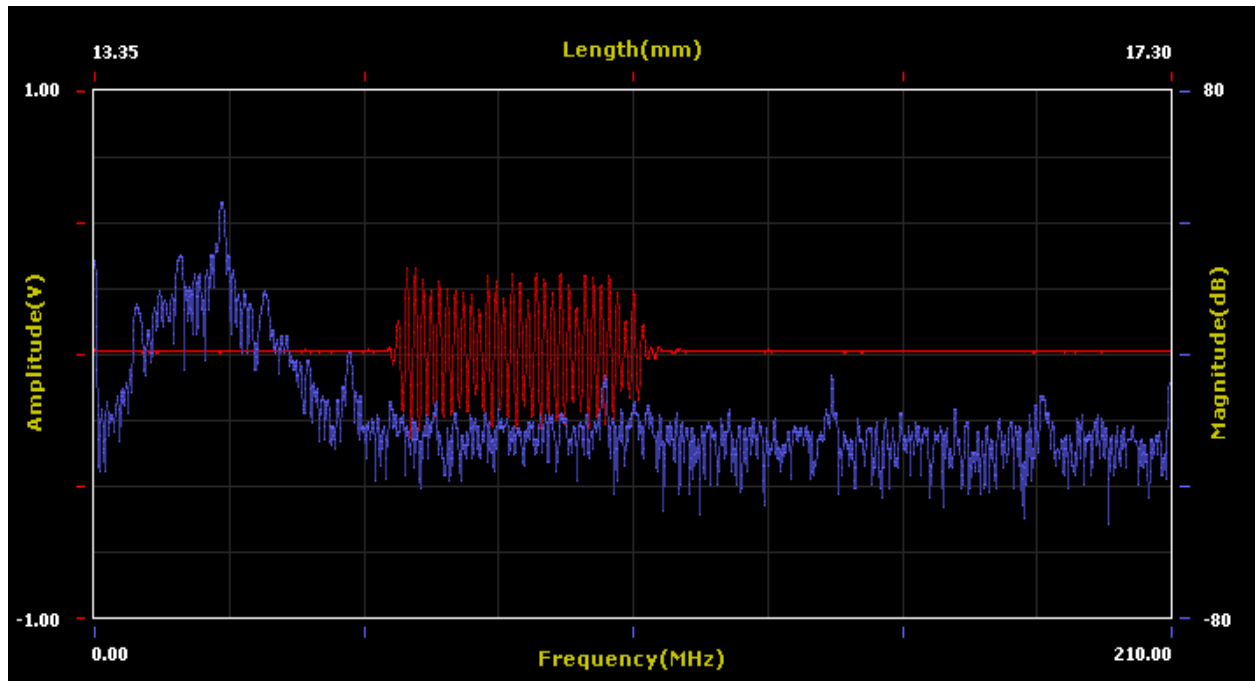
Figure 3.18: Measured period three backscattered signal (red) from insonating an Artenga bubble and its power spectrum (blue). The transmit pulse has a frequency of 25 MHz, pressure amplitude of 1.25 MPa and is 30 cycles long.
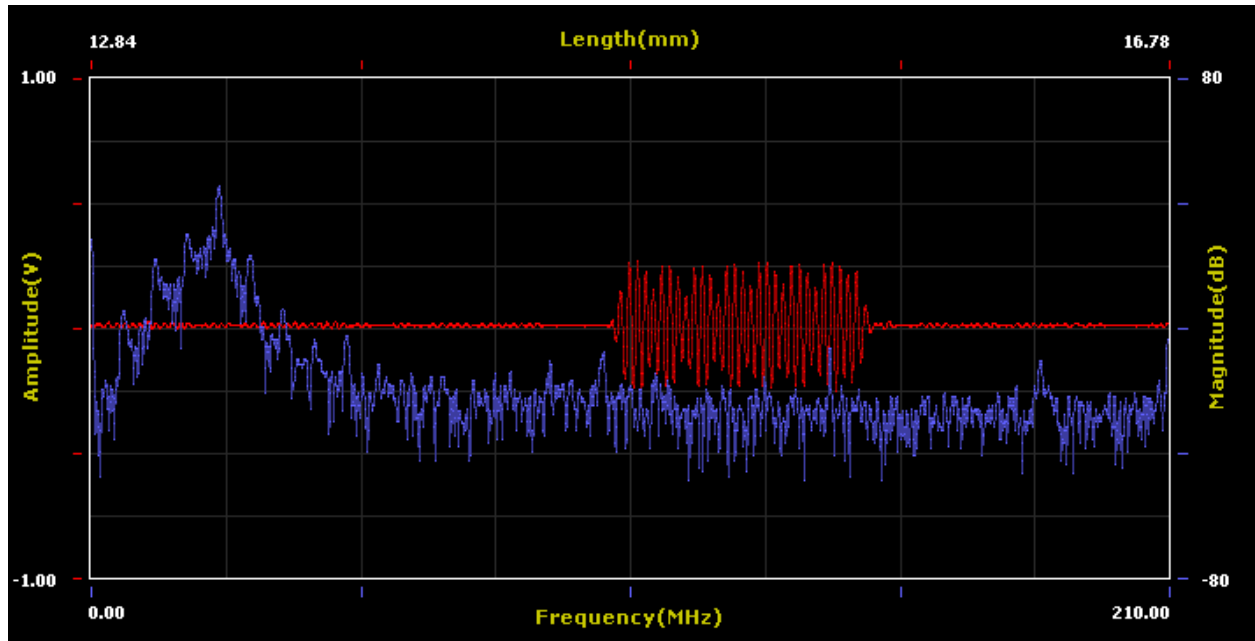
Figure 3.19: Measured period four backscattered signal from insonating an Artenga bubble (red) and its frequency spectrum (blue). The transmit pulse has a frequency of 25 MHz, pressure amplitude of 1.25 MPa and is 30 cycles long.
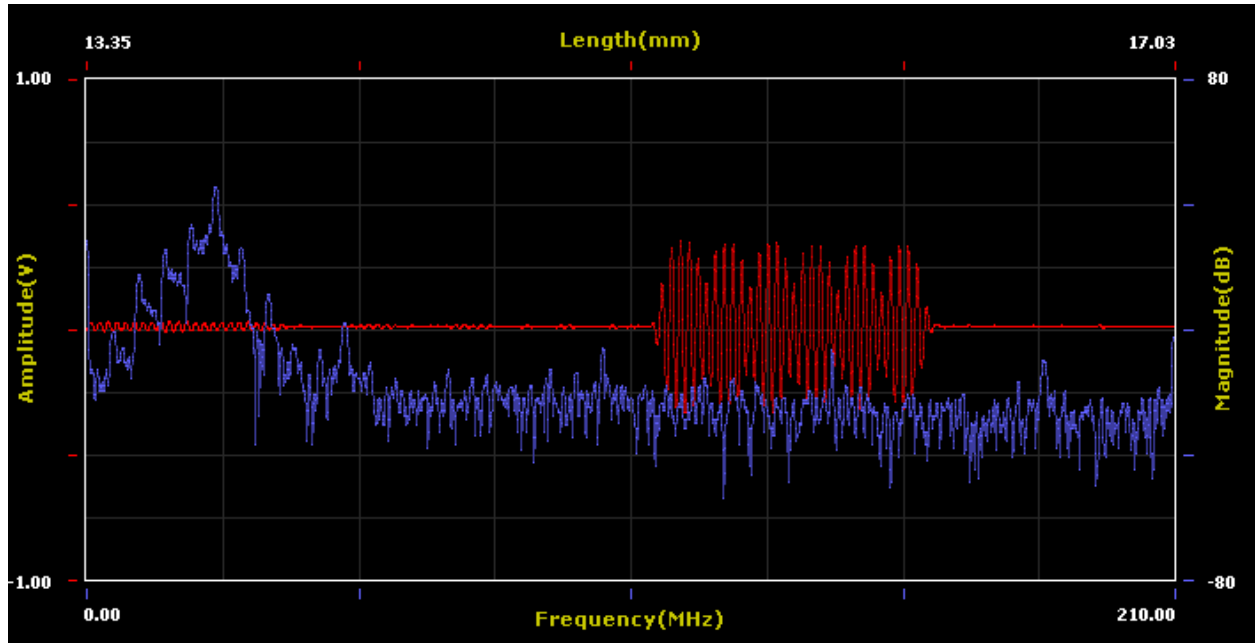
Figure 3.20: Measured period five backscattered signal from insonating an Artenga bubble (red) and its frequency spectrum (blue). The transmit pulse has a frequency of 25 MHz, pressure amplitude of 1.25 MPa and is 30 cycles long.

3.3 Ring down analysis

Results presented in section 3.2 showed that subpopulations of bubbles were able to exhibit the behavior predicted by numerical simulations. These behaviors include the subharmonics of higher order (period 3, period 4 and period 5 oscillations). According to the theoretical simulations, for bubbles to generate such subharmonics, the bubble should a) be insonated with a frequency which is equal or slightly less than integer multiples of its resonance frequency (e.g. 2.8 times the resonance frequency of the bubble to get period 3 oscillations, Figure 3.6) and b) sufficient pressure amplitude should be applied (Figures 3.1, 3.4, 3.7, 3.10). The results of Figure 3.13 suggest that these bubble oscillations associated with subharmonics are very sensitive to the initial bubble radius.

In order to experimentally confirm the resonance predictions by the model, the initial bubble radius need to be known or estimated. To achieve this, the free oscillations of the bubbles were studied (section 2.1.4). After turning off the acoustic driving pulse, the bubble oscillates for a limited number of cycles. The frequency of these free oscillations is equal to the resonance frequency of the bubbles (Leighton 1994). Appropriate period 2, period 3, period 4 and period 5 signals were selected which were able to fully satisfy the constraints listed in section 2.3.. In order to isolate the ring down oscillations the number of the driving cycles should be identified. In our experiments with DC710 oil as a reflecting surface (Figure 3.14), it was found that for a 30 cycle input excitation there are 2 extra cycles, attributed to the transducer response. To isolate the free oscillations from the forced oscillations due to the incident pulse including the transducer response, the analysis window did not include signal from the first 32 cycles of the backscattered pulse. In addition, in order to separate the ring down backscattered signal from the noise, signals with a SNR of less than ~12.7dB were eliminated. Selected signals were multiplied by a signal with a rectangular window with amplitude of 1. The location of the window for the ring-down analysis starts after 32 cycles of the received backscatter signal with a length of approximately 2-3 cycles after which the ring down amplitude diminishes to less than 12.7dB above the noise level.

Figure 3.21 shows the extracted period 2 signal resulting from insonation of Artenga bubbles with 25 MHz pulse consisting of 30 cycles. The frequency content of the signal is shown in In Figure 3.22 the amplitude of each frequency is normalized to the fundamental frequency of the received signal. There is a clear subharmonic signal at 12.5 MHz.

Figure 3.23 illustrates the isolated ringdown signal from the bubble shown in Figure 3.21 (selected from the highlighted area) while the power spectrum of this segment is shown in Figure

3.24. The main frequency of the free oscillations is equal to 13 MHz, which is in line with numerical predictions. According to the numerical simulations if the bubble is sonicated with a frequency which is slightly less than m (2,3,4…) times its natural resonance frequency, and for sufficient pressure amplitude a subharmonics of order $\frac{1}{m}$ ... $\frac{m-1}{m}$ are observable in the backscatterd signal spectrum.

Figures 3.25 and 3.26 show the extracted period 3 signal and its frequency components. Two subharmonic components are detected at 8.33 MHz and 16.66 MHz. The ring down oscillations were isolated and are shown in Figure 3.27. The power spectrum of the free oscillations is depicted in Figure 3.28. The main frequency of the free oscillations is 8.38 MHz which is in line with theory which predicts a resonance frequency of 8.33 MHz or slightly higher. According to numerical simulations if the sonication frequency is slightly less than three times the natural resonance frequency of the bubble and for sufficient pressure amplitude the bubble is able to generate subharmonics of order 1/3 and 2/3 in the backscattered signal.

Out of the 64 signals collected for ring down analysis, 21 met the criteria for the ring down analysis outlined in the methods section. Of these 21, 11 were period 2 signals and 10 were period 3 signals. No period 4 and 5 signals met the criteria due to very weak ring- down signals. The reason for the weak signals might be the decreased sensitivity of the transducer in detecting lower frequencies of around 6.25 and 5 MHz. Out of those 11 period two signals the ring down analysis showed that the resonance frequency of the bubbles capable of exhibiting period two oscillations was 14.53±3.02 MHz which is consistent the numerical simulations. Analysis of 10 period three signals resulted in a resonance frequency of 9.53±1.37 MHz which is again consistent with the results of the numerical simulation.
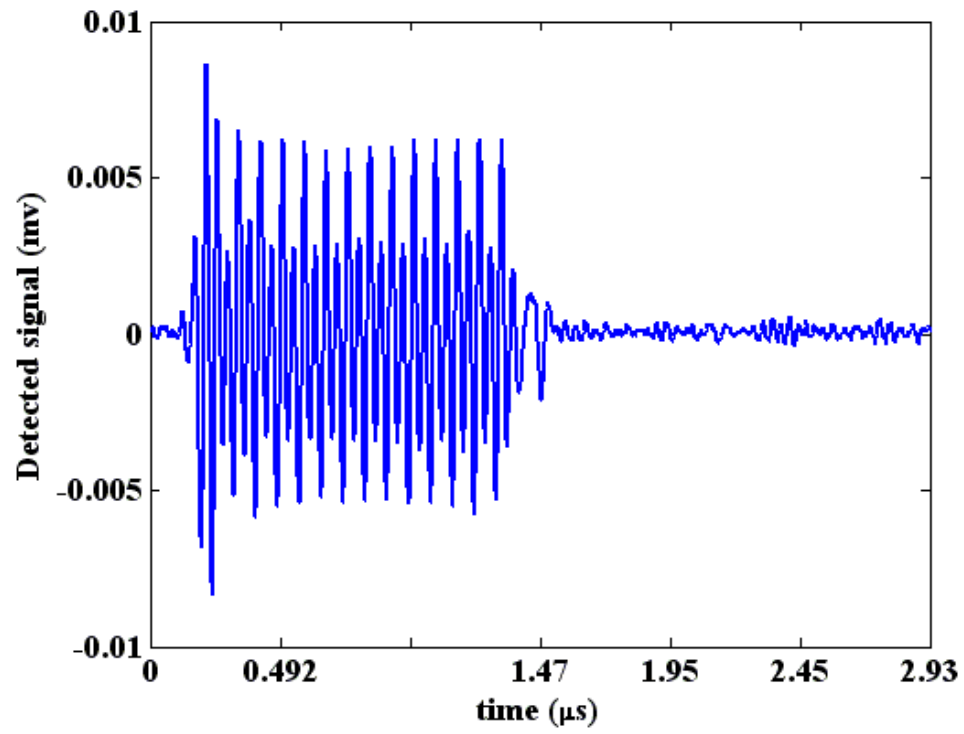
Figure 3.21: A measured period two backscattered signal from insonating insonating an Artenga bubble (pulse transmit frequency of 25 MHz, pressure amplitude of 1.25 MPa and 30 cycle length).
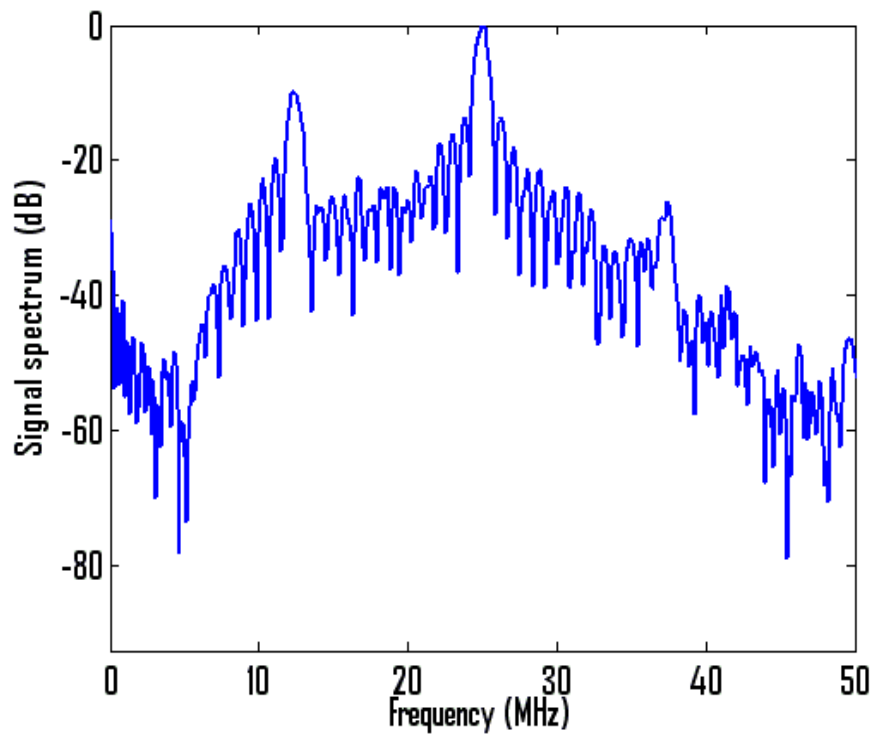
Figure 3.22: Power spectrum of the signal in figure 3.21. A strong subharmonic signal is detected at 12.5

MHz.
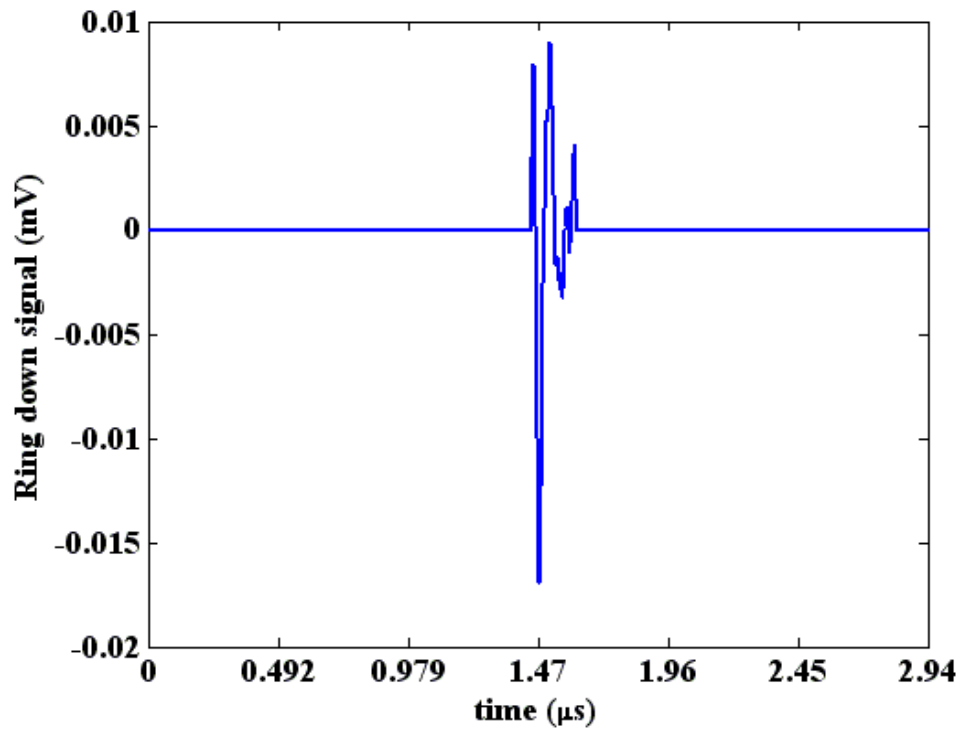
Figure 3.23: Ring down oscillations of the bubble (figure 3.21) after multiplying the signal by a rectangular window of amplitude 1 and appropriate width and position (determined according to the criteria outlined in section 2.2.4).
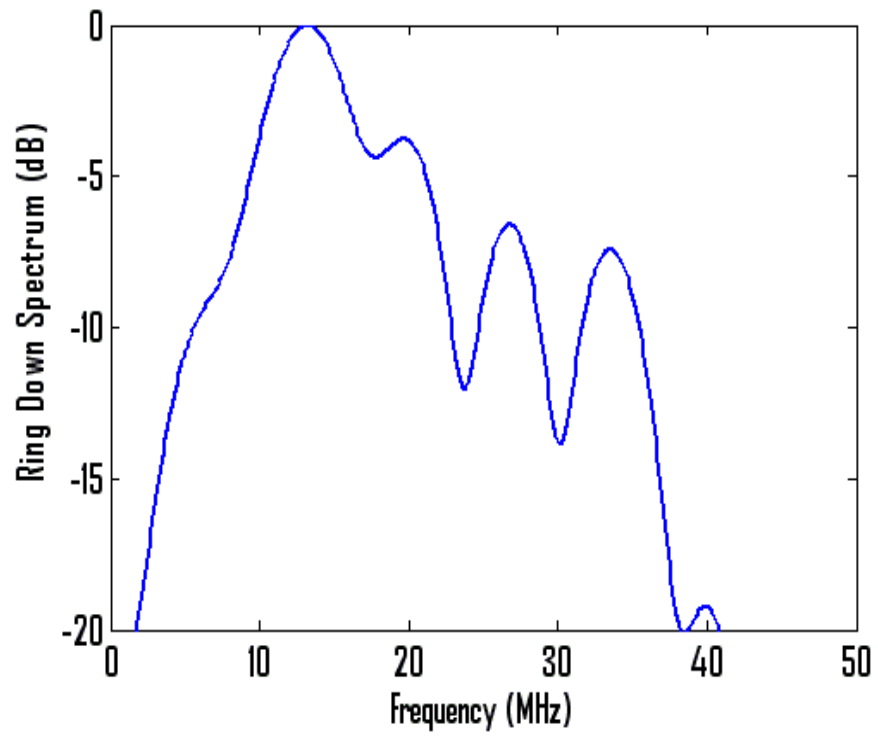
Figure 3.24: Power spectrum of the ring-down signal in figure 3.23.The ring-down is associated with a dominant 13 MHz oscillation frequency.
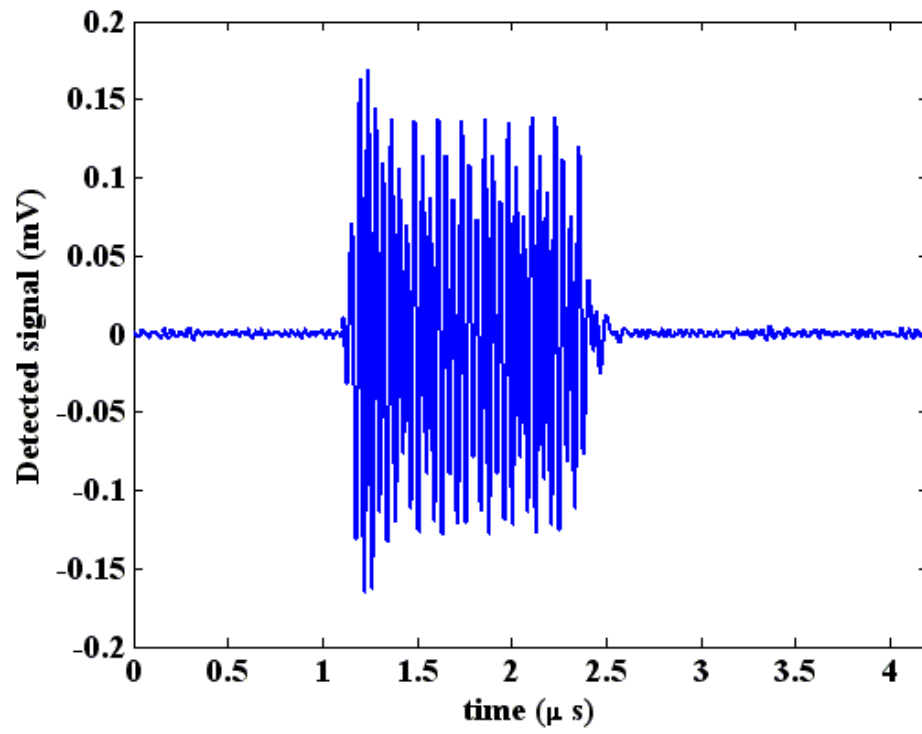
Figure 3.25: A measured period three backscattered signal from insonating an Artenga bubble (pulse transmit frequency of 25 MHz, pressure amplitude of 1.25 MPa and 30 cycle length).
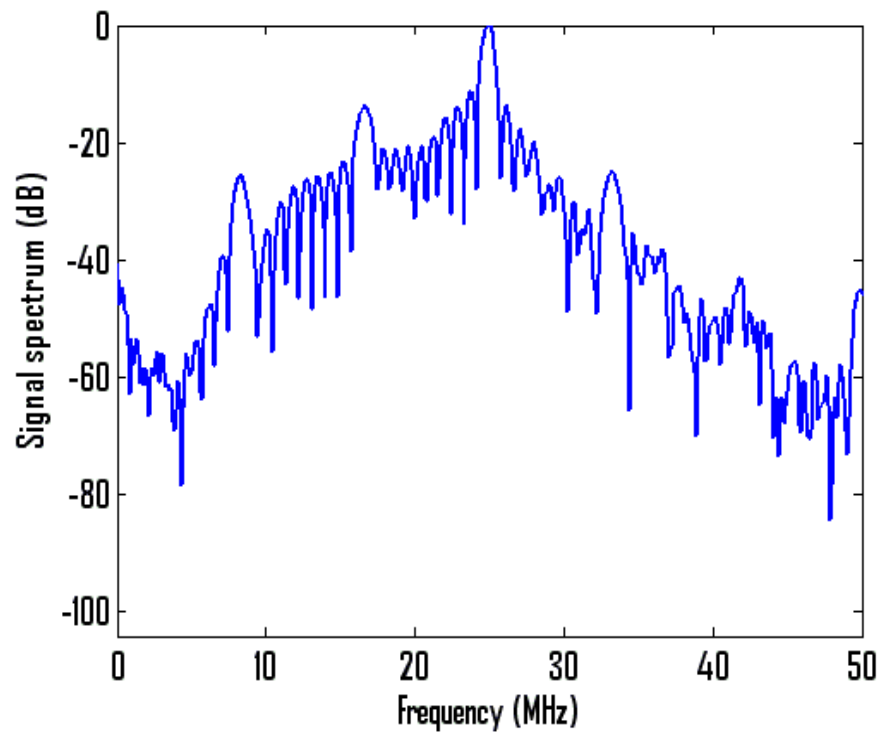
Figure 3.26: Power spectrum of the signal in figure 3.25.
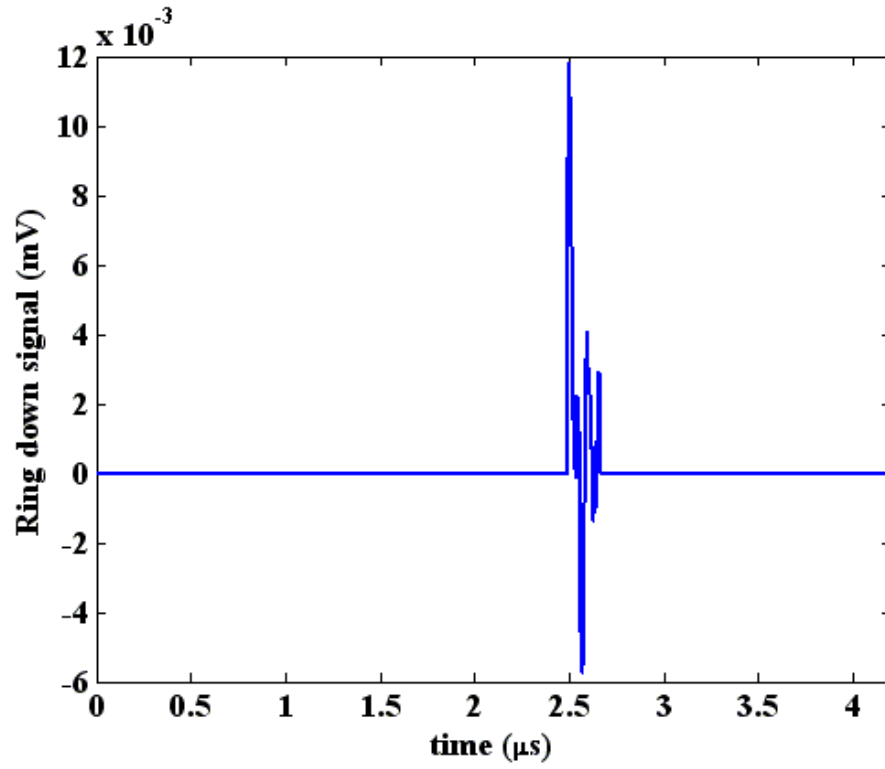
Figure 3.27: Ring down oscillations of the bubble in figure 3.25 after multiplying the signal by a rectangular window of amplitude 1 and appropriate width and position.
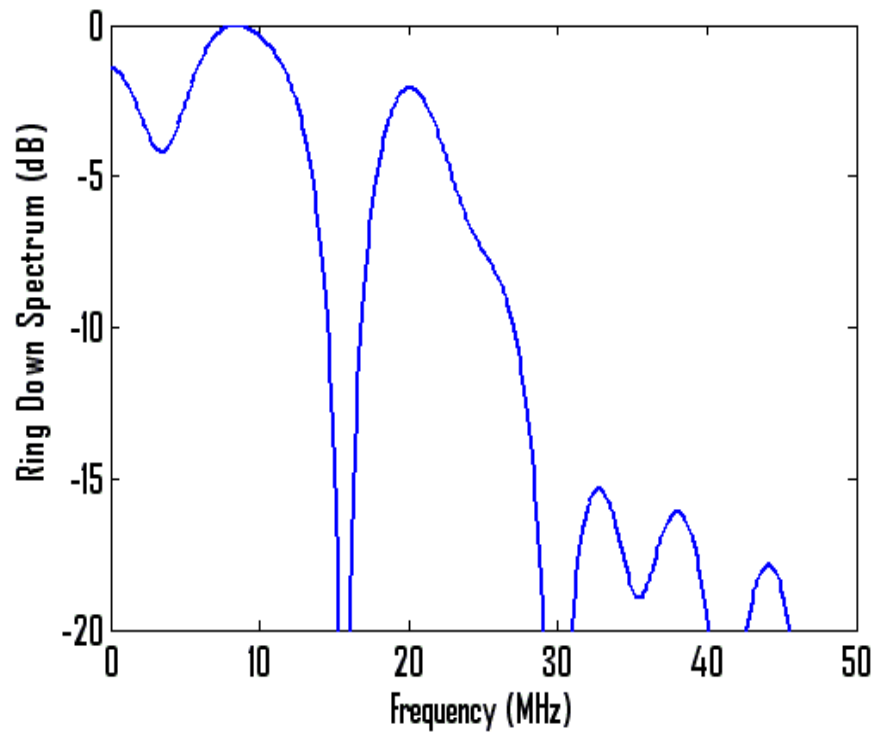
Figure 3.28: Frequency spectrum of the ring down oscillations in figure 3.26

Chapter 4 Discussion

4.1 Summary and discussion of the numerical and experimental results

The dynamics of the ultrasound contrast agents were studied for a wide range of system control parameters (including pressure, bubble size and frequency) both experimentally and theoretically. For both the theoretical and the experimental part of this study a novel and efficient method was employed to investigate the UCA dynamics. In the theoretical section, the use of the bifurcation diagrams enabled us to visualize the bubble behavior for a very wide range of the control parameters. This tool was used, for the first time, to classify the dynamics of the bubble in terms of its resonance frequency. Experimental methods were developed that permitted the sonication of a polydisperse solution of UCAs with different sizes and the isolation and analysis of signals from single bubbles. The efficient method of ringdown analysis (has also been used in (Sun et al. 2005)) enabled us to estimate the bubble natural resonance frequency based on the received signal and to test the theoretical predictions for a wide range of resonant frequencies and therefore bubble sizes. Through the combination of the parametric analysis of the bubble dynamics through the use of bifurcation diagrams and the experimental investigation of the UCA behavior, a more detailed insight into the behavior of microbubbles was obtained which was not available before.

According to our results, in addition to the generation of subharmonics at half of the driving acoustic frequency, it is possible to force the bubbles to exhibit higher subharmonics. In conventional subharmonic imaging the bubbles are insonated with a frequency of approximately twice their natural resonance frequency. If the pressure amplitude of the incident ultrasound is sufficient, the bubble will exhibit subharmonic oscillations at half the driving frequency.

Using the analysis tools presented in the thesis, we showed that if the bubble is insonated with a frequency more than twice its resonance frequency and slightly less than integer multiples of its resonance frequency (m=3,4,5,..) the bubble is able to exhibit subharmonics at higher order in its backscattered pressure. The strongest subharmonic will be of (m-1)/m order and has a higher frequency compared to the subharmonic at order ½.

Polydisperse populations of Artenga bubbles were insonated using a Vevo 770 at 25 MHz by applying sinusoidal pulses with 30 cycle length. Period two, three, four and five oscillations were detected. The frequency analysis of the detected signals showed that in addition to the conventional subharmonics at 12.5 MHz, the bubbles were able to exhibit higher subharmonics at 8.33 and 16.66 MHz for period three backscattered signals, 6.25, 12.5 and 18.75 MHz for the period four backscattered signals and 5,10,15 and 20 MHz for period five backscattered signals.

4.2 Summary and discussion of the ring down analysis

In order to further confirm the theoretical predictions regarding the generation of higher subharmonics, the frequency of the free oscillation of the bubbles was examined. As the frequency of the free oscillations should be at the natural resonance frequency of the bubbles, the validity of the theoretical predictions was tested. It was shown that both for the period two and period three oscillations the resonance frequency of the bubble is in the range of the

corresponding resonance frequency predicted by the numerical simulations. The results of the analysis of 11 period two signals showed that the resonance frequency of the bubbles capable of exhibiting period two oscillations was14.53±3.018 MHz which confirms the predictions of the numerical simulations. Analysis of 10 period three signals resulted in a resonance frequency of 9.53±1.37 MHz which is again consistent with the results of the numerical simulation. According to numerical simulations, in order to generate period three oscillations the sonication frequency should be equal to three times or slightly less than three times the natural resonance frequency of the bubbles. The analysis of the period 5 and period four signals were difficult as none of the ring-down oscillations were able to satisfy the SNR constraint. In other words, ring-down oscillations were not separable from the noise floor. We hypothesize this is due to the decreased sensitivity of the 25 MHz transducer in detecting the 6.25 and the 5 MHz oscillations, as they outside the transducer bandwidth.

4.3 possible applications of the observed phenomenon

In most of the imaging applications the driving frequency is chosen to be equal to the resonance frequency of the transducer to achieve the highest sensitivity. In conventional subharmonic imaging, the received signal from bubbles is detected at half the driving frequency. Because this frequency is far from the resonance frequency of the transducer, the transducer sensitivity at the subharmonic frequencies is low (This is only true if the transmit frequency is chosen to be the resonance frequency of the transducer). This may impair the detection of the weaker subharmonic signals in the regions of low blood flow as the number of the present bubbles is smaller and therefore the total resulting signal may be weaker.

In this work, we demonstrated theoretically and experimentally the existence of higher subharmonics. These subharmonics are of (m-1)/m order. As the integer m increases, the

frequencies of the subharmonics generated approach the resonant frequency of the transducer. Since the higher subharmonics are closer to the resonant frequency of the transducer, the sensitivity of the imaging device in detecting the backscattered signal increases. The maximum number of m achieved in our experiments is five. However, higher order subharmonics may be achievable at different acoustic conditions (higher pressures, frequencies or different type of UCAs). Compared to the conventional subharmonic imaging, this may result in a better SNR and sensitivity, depending on several factors. It should be noted that the above comparison is based on the assumption that the transmit frequency is at the resonance frequency of the transducer. However, a more reliable comparison should take into account the fact that the transmit frequency can be chosen not be equal to the resonance frequency of the transducer. (e.g. between the resonance frequency of the transducer and the sub harmonic frequency). In this case we need to do more rigorous and detailed analysis to achieve a more reliable comparison. Moreover, for the same number of transmit cycles, the higher frequency of the higher order subharmonics improves the imaging resolution (both axial and lateral).

The increase in resolution may be applied in two different approaches. Imagine an imaging system which operates at the frequency f (e.g. 4 MHz). This frequency is twice the resonance frequency of the employed bubbles. By tuning the frequency to a higher frequency and applying a sufficient pressure, the bubbles will be able to emit higher subharmonics. As an example by maintaining the number of cycles and increasing the frequency to 2f (8 MHz), and detecting the ¾ order subharmonics at 12f/4 (3/4*4f) (e.g. 6 MHz) the resolution of the system (both axial and lateral) is significantly improved compared to detecting at f (½*2f) (e. g. 2 MHz). For example imagine a pulse consisting of 8 cycles. The axial resolution of the ¾ order subharmonic and ½ order subharmonic can be calculated using:

$$Axial\ resolution = \frac{spatial\ pulse\ length}{2}$$

Where the spatial pulse length can easily be calculated using:

$$Spatial\ pulse\ length = \frac{speed\ of\ sound * number\ of\ cycles}{frequency}$$

Therefore the spatial pulse length for the ¾ order subharmonic will be 2 mm while the spatial resolution belonging to the ½ order subharmonic will be 6 mm. It should be noted that for simplicity of comparison, the assumption here is that we can generate higher order subharmonics with the same number of cycles necessary to generate 1/2 order subharmonics. However, in practice the number of cycles may not be equal and further detailed analysis is necessary to compare the axial resolutions. In addition the frequency of the higher order subharmonic is closer to the transmit frequency and assuming the transmit frequency to be equal to the resonance frequency of the transducer; the SNR will increase. Again the assumption here is that the transmit frequency is at the resonance frequency of the transducer. However, this may not always be true and for cases where the transmit frequency is not at the resonance frequency of the transducer, further comparison and analysis is needed to do the comparison. Another fact that should be considered in comparing the SNR is the absolute strength of the signal. In this regard the concenteration of the each population size should be considered. For example, if the number of UCAs emitting SH of 1/2 order is significantly higher than the number of bubbles emitting subharmonics of 3/4 order; the absolute strength of the 1/2 oredr subharmonic signal will be much higher than the 3/4 order subharmonic. Thus the SNR corresponding to 1/2 order subharmonic will be higher. This is another important fact that should be considered for further analysis in order to make more reliable comparisons between the SNR of different order subharmonics.

Despite the improved CTR, one drawback of the current subharmonic imaging of breast is the low frequency of insonation (4.4 MHz) (Forseberg et al. 2007; Eisenbrey et al. 2011) which decreases the resolution compared to the conventional B-mode breast scans at 9-12MHz (Athanasiou et al. 2009). However, through optimization of bubble size and properties using this approach, breast subharmonic imaging can potentially offer improved spatial resolution, both axial and lateral (considering the same imaging instrument, axial resolution will be improved if the number of transmit cycles is maintained. therefore, care must be taken in choosing the optimum number of cycles). In addition this technique combined with nonlinear frequency modulated ultrasound signals (Harput et al. 2010) will further improve the signal to noise and resolution.

Another approach is to use larger bubble sizes which have a lower resonance frequency. As an example, larger bubbles can be chosen, which have a resonant frequency of approximately one fourth of the driving frequency (1/4*f) suitable for high frequency subharmonic imaging. At 40 MHz and through applying a suitable pressure, the bubbles will emit higher subharmonics in the order of ¾ at 30 MHz. Compared to detection at f/2 (20 MHz), an improvement in spatial resolution is expected. One of the applications which may take advantage of this approach is high frequency subharmonic imaging (Goertz et al. 2005, 2006, 2007b, Needles et al. 2008). Despite the significant advantage of the subharmonic imaging at high frequencies in improving the CTR (Goertz et al. 2005), detection of the signals at half the driving frequency is not optimal; the detection sensitivity and resolution are reduced as the signal is usually at the limits of the useful transducer bandwidth. The conventional approach in high frequency subharmonic imaging is to filter the bubble sizes to smaller bubbles which have a resonance frequency at half the driving frequency (Shi et al. 1997, Shankar et al. 1998. Krishna et al. 1999, Forseberg et

al.2000). Through careful size selection of the bubbles and employing larger bubble sizes, these bubbles can be forced to emit higher subharmonics and improve the sensitivity and resolution.

Another important application of the investigated phenomenon may be in Amplitude Modulation (AM) techniques. Amplitude modulation techniques (Porter et al. 2003, Brock-Fisher et al. 2006) are based on transmitting two pulses, one pulse usually having twice the amplitude of the second pulse. Upon scaling and subtraction of the backscattered signals, the residual of a linear scatter like tissue will be minimal. This is because the linear scattered behaves linearly and near full cancellation will be obtained by multiplying the received signal from the half amplitude pulse by two and subtracting it from the received signal belonging to sonication with the full amplitude pulse. However, due to the nonlinear response of the bubble to the pressure increase, the two signals do not cancel after scaling and subtraction. Therefore there would remain a significant residual signal belonging to the bubble and the CTR will be improved.

As seen in the bifurcation diagrams, when the bubble is sonicated with the appropriate frequency (capable of generating higher subharmonics) the radial oscillations of the bubble undergo a sudden increase as the pressure amplitude is raised above a threshold value. By choosing the appropriate pressure amplitudes associated with the two pulses, large changes in the subharmonic backscatter can be achieved, and therefore the CTR. Figure 3.1 and 3.2 illustrates this; if for this scenario the first pulse is sent with an amplitude of 0.3 MPa, and the second with an amplitude of 0.6 MPa, large gains in CTR can be achieved. Therefore, setting the amplitudes of the amplitude modulation first and second pulses to be smaller and greater than the pressure threshold, the CTR of the amplitude modulation technique may be enhanced significantly. It has been recently shown that one way to increase the nonlinearity is to take advantage of the buckling behavior of lipid shell bubbles

(Emmer et al. 2007a). However, this method is limited to frequencies below the resonance of the bubble. To achieve enhanced nonlinearity at high frequencies, the oscillations of the UCAs should be optimized.

Chapter 5 Conclusion and future work

In conclusion, through both experimental and theoretical investigations, the feasibility of the generation of higher subharmonics was shown. It was confirmed that through careful resonace selection of bubbles (resonance frequency strongly depends on bubble size) and application of a frequency which is equal or slightly less than integer multiples of the resonance frequency of the bubbles (m = 3, 4 , …) and by applying a sufficiently high acoustic pressure, the bubbles can exhibit subharmonics of higher order. Because of the higher frequency content of the higher subharmonics the sensitivity and resolution of the procedure can potentially be improved compared to conventional subharmonic imaging. This may be beneficial in improving clinical breast subharmonic imaging and high frequency subharmonic scanning of small animals. This technique will increase the sensitivity of the measurement especially in case of the regions of small blood flow where weaker signals are expected due to the lower concentration of the bubbles.

This study had certain limitations. Long pulses consisting of 30 cycles were employed. The application of long cycles is not appropriate for clinical imaging as the axial resolution of the images decreases significantly. Long pulses were implemented in our since there will be a clear separation between the frequencies of the backscattered signal. This significantly helps us to test

the theoretical predictions and gain a clear insight into the bubble dynamics. As the aim of this study was to obtain a deeper understanding regarding the physics behind the bubble dynamics and classify their behavior, application of shorter cycles suitable for clinical applications was not investigated. However, for an actual subharmonic imaging procedure, the relationship between the number of the transmit cycles and the strength of the higher subharmonics is very important and should be studied. Generating stronger subharmonics through transmitting a shorter pulse is desirable as the axial resolution will significantly be improved. Investigation of the relationship between the cycles and the strength of higher subharmonics should be the subject of further study.

As the goal of this study was to investigate the dynamics of the bubble versus a wide range of the bubble sizes, we employed a polydisperse size distribution of Artenga bubbles. This made the determination of the pressure threshold for the generation of each of the higher periods regimes very difficult. Application of stacks of monodispers bubbles (e.g. through centrifuging a polydisperse solution (Feshtihan et al. 2009; Sirsi et al. 2010)) with resonance frequencies of 1/3, ¼ and 1/5 of the driving frequency and obtaining the pressure threshold for the generation of each of these higher subharmonics can be the subject of the future studies. Obtaining this pressure threshold can also aid in designing a more efficient amplitude modulation technique at higher frequencies.

Recently, the application of lipid shell bubbles like Definity has attracted a lot of interest in contrast enhanced ultrasound imaging. The softer shell leads to a buckling behavior specific to lipid shell bubbles. Therefore, the generation of nonlinear signals is much easier and may be possible at lower pressures (de Jong et al. 2007; Emmer et al. 2009, 2007a,2007b,2007c; Frinking et al. 2010;Faez et al. 2011). The majority of the bubbles used in our studies were

surfactant shell Artenga bubbles. The theoretical model (Hoff model) employed in numerical simulations is suitable for only viscoselastic shells and is not able to simulate the more intricate behavior of the lipid shell bubbles (such as buckling). Employing the buckling phenomenon in using new models (e. g. the Marmottant model (Marmottant et al. 2005)) and the classification of the dynamics of the lipid shell bubble at higher frequencies can be the subject of the future studies. In addition similar experiments can be performed on lipid bubbles to test these theoretical predictions.

Bibliography

Athanasiou, A., Tardivon, A., Ollivier, L., Thibault, F., Khoury., C.E., Neuenschwander, S. (2009). How to optimize breast ultrasound. European Journal of Radiology, 69(1), 6-13.

Behnia S., Jafari, A., Soltanpoor, W., and Jahanbakhsh, O. (2009). Nonlinear transitions of a spherical cavitation bubble. Chaos, Solitons & Fractals, 41, 818-828.

Behnia, S., Jafari., A., Soltanpoor, W., and Sarkhosh, L. (2009). Towards classification of the bifurcation structure of a spherical cavitation bubble. Ultrasonics, 49, 605-610.

Bekeredjian, R., Chen, S., Frenkel, P.A., Grayburn, P.A., and Shohet, R.V. (2003). Ultrasound-targeted microbubble destruction can repeatedly direct highly specific plasmid expression to the heart. Circulation, 108, 1022–1226.

Bhagavatheeshwaran, G., Shi, W.T., Forsberg, F., Shankar, P.M. (2004). Subharmonic signal generation from contrast agents in simulated neovessels. Ultrasound in Medicine & Biology, 30(2), 199-203.

Biagi, E., Breschi, L., and Masotti, L. (2005). Transient Subharmonic and Ultraharmonic Acoustic Emission During Dissolution of Free Gas Bubbles. IEEE Transactions on Ultrasonics, Ferroelectrics, and Frequency Control, 52(6), 1048-1054.

Boccara, N. (2004). Modeling complex systems, Springer-Verlag, New York.

Brock-Fisher, G. A., and Prater, D.M. (2006). Acoustic border detection using power modulation US Patent no 06997875 (Koninklijke Philips Electronics N.V.)

Burns, P.N., Wilson, S.R. and Simpson, D.H. (2000). Pulse inversion imaging of liver blood flow—improved method for characterizing focal masses with microbubble contrast Invest. Radiol., 35, 58–71.

Burns, P.N., Powers, J.E., Fritzsch, T. (1992). Harmonic imaging: A new imaging and Doppler method for contrast enhanced ultrasound. Radiology, 185,142.

Calliada, F., et al. (1998). Ultrasound contrast agents Basic principles. European Journal of Radiology, 27, S157-S160.

Chang, P.H., Shung K.K., and Levene HB. (1996). Quantitative measurements of second harmonic Doppler using ultrasound contrast agents, Ultrasound in Medicine and Biology, 22, 1205–1214.

Chang, P.H., Shung, K.K., Wu, S., and Levene, H.B. (1995). Second harmonic imaging and harmonic Doppler measurements with Albunex. IEEE Trans. Ultrason. Ferroelec. Freq. Contr. 42, 1020–1027.

Cheung, K., Couture, O., Bevan, P.D., Cherin, E., Williams, R., Burns, P.N. and Foster, F.S. (2008). In vitro characterization of the subharmonic ultrasound signal from Definity microbubbles at high frequencies. Phys. Med. Biol., 53, 1209.

Chomas, J., Dayton, P., May, D., and Ferrara, K. (2002) Nondestructive Subharmonic Imaging. IEEE Transactions on Ultrasonics, Ferroelectrics, and Frequency Control, 49(7) , 883-892.

Church, C.C. (1995). The effects of an elastic solid surface layer on the radial pulsations of gas bubbles. J. Acoust. Soc. Am., 97, 1510.

Correas, J., Bridal, L., Lesavre, A., Mejean, A., Claudon, M., and Helenon, O. (2001). Ultrasound contrast agents: Properties, principles of action, tolerance and artifacts. Eur. Radiol., 11, 1316–1328.

Cosgrove, D. (2006). Ultrasound contrast agents: An overview. European Journal of Radiology, 60, 324-330.

Dayton, P.A., and Ferrara, K.W. (2002). Targeted imaging using ultrasound. J. Magn. Reson. Imag., 16, 362–377.

Dave, J.K., Forsberg, F., and Fernandes, S., et al. (2010). Static and dynamic cumulative maximum intensity display mode for subharmonic imaging – a comparative study with mammography and conventional ultrasound techniques. J. Ultrasound Med. 29, 1177–1185.

de Jong, N., Bouakaz, A., and Frinking. P. (2002). Basic Acoustic properties of microbubbles. Echocardiography, 19(3), 229-240.

de Jong, N., Cornet, R., Lancee, C.T. (1994). Higher harmonics of vibrating gas-filled microspheres. Part two: Measurements. Ultrasonics, 32, 455– 459.

de Jong, N., Emmer, M., Chin, C.T., Bouakaz, A., Mastik, F., Lohse, D., and Versluis, M. (2007). "Compression-Only" Behavior of Phospholipid-Coated Contrast Bubbles. Ultrasound in Medicine & Biology, 33(4), 653-656.

Deng, C.X., and Lizzi, F.L. (2002). A review of physical phenomena associated ultrasound contrast agents and illustrative clinical applications. Ultrasound Med. Biol., 28, 277–86.

Stride, E., and Saffari, N. (2003). Microbubble ultrasound contrast agents: A review. Proceedings of the Institution of Mechanical Engineers, Part H: Journal of Engineering in Medicine, 217, 429.

Eisenbrey, J.R., et al. (2011a). Simultaneous grayscale and subharmonic ultrasound imaging on a modified commercial scanner. Ultrasonics, 51(8), 890-897.

Eisenbrey J.R, Joshi, N., Dave1, J.K., and Forsberg, F. (2011b) Assessing algorithms for defining vascular architecture in subharmonic images of breast lesions. Physics in Medicine & Biology, 56, 919–930.

Eisenbrey, J.R., Dave J.K., Merton, D.A., Palazzo, J.P., Forsberg, F. (2011c). Parametric Imaging Using Subharmonic Signals From Ultrasound Contrast Agents in Patients With Breast Lesions. Journal of Ultraound in Medicine, 30(1), 85-92.

Eller, A., and Flynn, H.G. (1969). Generation of subharmonics of order one-half by bubbles in a sound field. J. Acoust. Soc. Am., 46, 722–7.

Emmer, M., van Wamel, A., Goertz, D.E., de Jong, N. (2007a). The Onset of Microbubble Vibration. Ultrasound in Medicine & Biology, 33(6), 941-949.

Emmer, M., Vos, H.J., van Wamel, A., Goertz, D.E., Versluis, M., de Jong, N. (2007b). Clinical relevance of pressure-dependent scattering at low acoustic pressures   Ultrasonics, 47(1-4), 74-77.

Emmer, M., Vos, H.J., Goertz, D.E., van Wamel, A., Versluis, M., de Jong, N. (2009). Pressure-Dependent Attenuation and Scattering of Phospholipid-Coated Microbubbles at Low Acoustic Pressures. Ultrasound in Medicine & Biology, 35(1), 102-111.

Esche, R. (1952). Untersuchungder schwingungs kavitation in flussigkeiten. Acustica, 2,208-218.

Faez, T., Emmer, M., Docter, M., Sijl, J., Versluis, M., de Jong, N. (2011). Characterizing the Subharmonic Response of Phospholipid-Coated Microbubbles for Carotid Imaging. Ultrasound in Medicine & Biology, 37(6), 958-970.

Falou, O., Baddour, R.E., Nathanael, G., Czarnota, G.J., Kumaradas, J.C. and Kolios, M.C. (2008) A study of high frequency ultrasound scattering from non-nucleated biological specimens.The Journal of the Acoustical Society of America, 124(5): EL278-EL283.

Ferrara, K.W., Meritt, C.R., Burns, P.N., Foster F.S., Mattrey, R.F. and Wickline, S.A. (2000). Evaluation of tumor angiogenesis with US: Imaging, doppler and contrast agents, Acad Radiol, 7, 824–839.

Ferrara, N. & Kerbel, R.S. (2005). Angiogenesis as a therapeutic target. Nature, 438(15), 967-974.

Feshitan, J., Chen, C.C., Kwan, J.J., and Borden, M.A. (2009). Microbubble size isolation by differential centrifugation. J. Colloid. Interface. Sci., 329, 316–324.

Flynn, H.G., and Church C.C. (1988). Transient pulsations of small gas bubbles in water. Journal of the Acoustical Society of America, 84, 985-998.

Forsberg, F., Shi, W.T. and Goldberg, B.B. (2000). Subharmonic imaging of contrast agents. Ultrasonics, 38, 93-98.

Forsberg, F., Goldberg, B.B., Liu, J.B., Merton, D.A., and Rawool, N.M. (1996). On the feasibility of real-time, in vivo harmonic imaging with proteinaceous microspheres. J. Ultrasound. Med., 15, 853–860.

Forsberg, F., Goldberg, B.B, Wu, Y.Q., Liu, J.B., Merton, D.A., and Rawool, N.M. (1997). Harmonic imaging with gas-filled microspheres: Initial experiences. Int. J. Imaging. Syst. Tech., 8, 69–81.

Forsberg, F., Shi, W.T., Goldberg, B.B. (2000), Subharmonic imaging of contrast agents Ultrasonics, 38, 93-98.

Forsberg, F., Liu, J.B., and Shi, W.T. et al. (2006). In vivo perfusion estimation using subharmonic contrast microbubble signals. J. Ultrasound Med., 25, 15–21.

Forsberg, F., Piccoli, C.W., Merton, D.A., Palazzo, J.J., and Hall, A.L. (2007a). Breast Lesions: Imaging with Contrast-enhanced Subharmonic US—Initial Experience1. Radiology, 244(3), 718-726.

Forsberg, F., Piccoli, C., and Merton. D.A. et al. (2007b). Breast lesions: Imaging with contrast-enhanced subharmonic US-initial experience. Radiology, 244 718–726.

Foster, F.S., Pavlin, C.J., Harasiewicz, K.A., Christopher, D.A. and Turnbull, D.H. (2000). Advances in ultrasound biomicroscopy. Ultrasound. Med. Biol., 26, 1–27.

Frinking, P.J.A, Bouakaz, A., Kirkhorn, J., Cate, F.J. and de Jong, N. (2000). Ultrasound contrast imaging: Current and new potential methods. Ultrasound. Med. Biol., 26, 965–975.

Frinking, P.J.A, Gaud, E., Brochot, J., Arditi, M. (2010). Subharmonic scattering of phospholipid-shell microbubbles at low acoustic pressure amplitudes. IEEE Transactions on Ultrasonics, Ferroelectrics, and Frequency Control, 57(8), 1762-1771.

Gasparini, G., and Harris, A.L. (1995). Clinical importance of the determination of tumor angiogenesis in breast carcinoma: much more than a new prognostic tool. J. Clin. Oncol., 13, 765–782.

Goertz, D.E., Christopher, D.A., Yu, J.L., Kerbel, R.S., Burns, P.N., and Foster, F.S. (2000) High frequency color flow imaging of the microcirculation," Ultrasound Med. Biol., vol. 26, 63–71.

Goertz, D.E. (2002) Imaging the Microcirculation with High Frequency Ultrasound. (Toronto: University of Toronto)

Goertz, D.E., Frijlink, M., Bouakaz, A., Chin, C.T., de Jong, N. and van der Steen, A. (2003a) The effect of bubble size on nonlinear scattering from microbubbles. IEEE Ultrasonics Symp. (Hawaii, USA), 1503–1506.

85

Goertz, D.E., Yu, J.L., Kerbel, R.S., Burns, P.N., and Foster, F.S. (2003b). High frequency 3D imaging of the microcirculation. Ultrasound Med. Biol., 29, 39–51.

Goertz, D.E., Frijlink, M., de Jong, N., and van der Steen, A. (2004). High frequency nonlinear scattering and imaging of a submicron contrast agent IEEE UFFC (Montreal, Canada), 986–989.

Goertz, D. E., Cherin, E., Needles, A., Karshafian, R., Brown, A.S., Burns, P.N. and Foster, F.S. (2005). High frequency nonlinear B-scan imaging of microbubble contrast agents IEEE Trans. Ultrason. Ferroelectr. Freq. Control, 52, 65–79.

Goertz, D.E., Frijlink, M.E., de Jong, N. and van der Steen, A.F. (2006a). High frequency nonlinear scattering from a micrometer to submicrometer sized lipid encapsulated contrast agent. Ultrasound Med. Biol., 32, 569–577.

Goertz, D.E, Frijlink, M.E., de Jong , N., and van der Steen, A.F. (2006b) Nonlinear intravascular ultrasound contrast imaging. Ultrasound Med. Biol., 32, 491–502.

Goertz D.E., de Jong, N. and van der Steen, A.F. (2007a) Attenuation and size distribution measurements of definity (TM) and manipulated definity (TM) populations Ultrasound. Med. Biol., 33, 1376–1388.

Goertz DE, Frijlink ME, Tempel D, Bhagwandas V, Gisolf A, Krams R, de Jong N, van der Steen AFW. (2007b). Subharmonic Contrast Intravascular Ultrasound for Vasa Vasorum Imaging. Ultrasound in Medicine & Biology, 33(12), 1859-1872.

Goldberg, B.B., Raichlen, J.S., and Forsberg, F. (2001) Ultrasound Contrast Agents: Basic Principles and Clinical Applications. 2nd Ed, Martin Dunitz Ltd, London.

Goldberg, B.B., Liu, J.B., Burns, P.N. et al. (1993). Galactose-based intravenous sonographic contrast agent: Experimental studies. J. Ultrasound Med. 12, 463–470.

Gong, Y., Cobbadi, M., and Porter, T.M. (2010) Relationship between size and frequency dependent ttenuation of monodisperse populations of lipid coated microbubbles. Bubble Science, Engineering and Technology, 2, 41-47.

Gramiak, P.M. Shah and D.H., Kramer. (1969) Ultrasound cardiography: contrast study in anatomy and function. Radiology, 92, 939–948.

Harput, S., Arif, M., and Freear, S.(2010) Experimental Investigation of the Subharmonic Emission from Microbubbles using Linear and Nonlinear Frequency Modulated Signals. 2010 IEEE International Ultrasonics Symposium Proceedings, 1724-1727.

Harvey, C.J., Blomley, M.J.K., Eckersley, R.J., and Cosgrove D.O.(2001). Developments in ultrasound contrast media, European Radiology.11(4),675-689.

Hilgenfeldt, S., Lohse, D., and Zomack, M. (2000). Sound scattering and localized heat deposition of pulse-driven microbubbles. J. Acoust. Soc. Am., 107(6), 3530-3539.

Hitchcock, K.E., and Holland, C.K. (2010) Ultrasound-Assisted Thrombolysis for Stroke Therapy : Better Thrombus Break-Up With Bubbles. Stroke, 41, S50-S53.

Hoff, L., Sontum, P.C., and Hovem, J.M. (2000) Oscillations of polymeric microbubbles: Effect of the encapsulating shell. J. Acoust. Soc. Am., 107(4), 2272-2280.

Holt, R.G., and Roy, R.A. (2001). Measurements of bubble-enhanced heating from focused, MHz-frequency ultrasound in a tissue-mimicking material. Ultrasound in Medicine & Biology, 27(10), 1399-1412.

Holt, R.G., Gaitan, D.F., Atchley, A.A., and Holzfuss, J. (1994). Chaotic sonoluminescence. Phys. Rev. Lett., 72(9), 1376-1379.

Iradji, S. (2008). Optimization of subharmonic generation from ultrasound contrast agents at high frequency ultrasound Master Thesis, Ryerson University, Toronto, Canada)

Kerbel, R.S., (2001). Clinical trials of antiangiogenic drugs: opportunities, problems, and assessment of initial results. J. Clin. Oncol., 19, 45S–51S.

Kerbel, R.S. (2006). Antiangiogenic theraphy: a universal chemosensitization strategy for cancer Science, 312, 1171–1175.

Klibanov, A.L. (2007). Ultrasound molecular imaging with targeted microbubble contrast agents. J. Nucl. Cardiol., 14, 876–884.

Kopans, D.B. (1998). Breast Imaging 2nd ed (Philadelphia, PA: Lippincott Williams & Wilkins).

Krishna, P.D., Shankar P.M., and Newhouse, V.L. (1999). Subharmonic generation from ultrasonic contrast agents. Phys. Med. Biol., 44, 681–694.

Kruse., D., Fornaris, R., Silverman, R., Coleman, D., and Ferrara, K. (1998). A swept-scanning mode for estimation of blood velocity in the microvasculature," IEEE Trans. Ultrason., Ferroelect., Freq. Contr., 45, 1437–1440.

Kruse, D. and Ferrara, K.W. (2002). A new high resolution color flow system using an eigen-decomposition based adaptive filter for clutter rejection. IEEE Trans. Ultrason., Ferroelect., Freq. Contr., 49, 1384–1399.

Kvikliene, A., Jurkonis, R., Ressner, M., Hoff, L., Jansson, T., Janerot-Sjberg, B., Lukoevicius, A. and Ask, P. (2004). Modelling of nonlinear effects and the response of ultrasound contrast micro bubbles: next term simulation and experiment. Ultrasonics, 42, 301-307.

Lanza, G.M. and Wickline, S.A. (2001). Targeted ultrasonic contrast agents for molecular imaging and therapy. Prog. Cardiovasc. Dis., 44, 13–31.

Lauterborn, W. (1976). Numerical investigation of nonlinear oscillations of gas bubbles in liquids. J. Acoust. Soc. Am., 59, 283–293.

Lauterborn, W., and Cramer, L. (1981). Subharmonic route to chaos observed in acoustics. Phys. Rev. Lett., 47(20),144-158.

Lauterborn W. and Suchla E. (1984) .Bifurction straucture in a model of acoustic turbulence. Phys. Rev. Lett., 53(24),2304-2307.

Lauterborn, W., and Koch, A. (1987). Holographic observation of period-doubled and chaotic bubble oscillations in acoustic cavitation. Phys. Rev. A., 35(4):1974-1976.

Lauterborn, W., Parlitz, U. (1988). Methods of chaos physics and their application to acoustics. J. Acoust. Soc. Am., 84(6):1975-1993.

Leighton, T.G. (1997). The acoustic bubble. (Academic Press Inc., London, UK).

Leodore, L.M., Forsberg, F., and Shi, W.T. (2007). In vitro pressure estimation obtained from subharmonic contrast microbubble signals. Proc. IEEE Ultrason. Symp. , 2207–2210

Lewin, P.A. (2004). Quo vadis medical ultrasound?. Ultrasonics, 42, 1–7.

Liu,Y., Miyoshi, H. and Nakamura, M. (2006). Encapsulated ultrasound microbubbles: therapeutic application in drug/gene delivery. J. Control. Release, 114, 89–99.

Lotsberg, O., Hovem, J.M., and Aksum, B., (1996). Experimental observation of subharmonic oscillations in infoson bubbles. J. Acoust. Soc. Am., 99, 1366–1369.

Marmottant, P., van der Meer S, Emmer M, Versluis M, de Jong N, Hilgenfeldt S, and Lohse D. (2005). A model for large amplitude oscillations of coated bubbles accounting for buckling and rupture. J. Acoust. Soc. Am., 118(6), 3499-3505.

Macdonald, C.A., and Gomatam, J. (2006) Chaotic dynamics of microbubbles in ultrasonic fields, Proc. IMechE., 220, 333-343.

Meairs, S., Alonso, A. (2007). Ultrasound, microbubbles and the blood–brain barrier. Progress in Biophysics and Molecular Biology, 93, 354-362.

Miles, K.A., Leggett, D.A., Kelley, B.B, et al. (1998). In vivo assessment of neovascularization of liver metastases using perfusion CT. Br. J. Radiol., 71, 276–281.

Mulvagh, S.L., Foley, D.A., Aeschbacher, B.C., Klarich, K.K., Seward, J.B.(1996).Second harmonic imaging of an intravenously administered echocardiographic contrast agent: Visualization of coronary arteries and measurement of coronary blood flow. Journal of the American College of Cardiology, 27, 1519-1525.

Mulvagh, S.L., DeMaria, A.N., Feinstein, S.B. et al. (2000) Contrast echocardiography: current and future applications. J. Am. Soc. Echocardiography, 13, 331-342.

Weidner, N., Folkman, J., Pozza, F., et al. (1992). Tumor angiogenesis: a new significant and independent prognostic indicator in early stage breast cancer. J. Natl. Cancer Inst., 84, 1875–1887.

Needles, A., Goertz D.E., Karshafian, R., Cherin, E., Brown, A.S., Burns, P.N., Foster, F.S. (2008). High-Frequency Subharmonic Pulsed-Wave Doppler and Color Flow Imaging of Microbubble Contrast Agents. Ultrasound in Medicine & Biology, 34(7), 1139-1151

F.S., Neppiras, E.A. (1968). Subharmonic and other low-frequency emission from bubbles in sound-irradiated liquids. J. Acoust. Soc. Am., 46, 587– 601.

Parlitz, U., Englisch, V., Scheffczyk, C., Lauterborn, W. (1990). Bifurcation structure of bubble oscillators. J. Acoust. Soc. Am. 88(2),1061-1077.

Phelps, A.D. and Leighton, T.G. (1997). The subharmonic oscillations and combination-frequency subharmonic emissions from a resonant bubble: their properties and generation mechanisms. Acustica, 83, 59–66.

Phillips, P., and Gardner, E. (2004). Contrast-agent detection and quantification Eur. Radiol., 14, P4–10.

Porter, T. R., Oberdorfer, J., Rafter, P., Lof, J. and Xie, F. (2003). Microbubble responses to a similar mechanical index with different real-time perfusion imaging techniques. Ultrasound Med. Biol., 29, 1187–1192.

Prosperetti, A. (1977). Application of the subharmonic threshold to the measurement of the damping of oscillating gas bubbles. J. Acoust. Soc. Am., 61,11–16.

Qin, S., Caskey, C.F., and Ferrara, K.W. (2009).Ultrasound contrast microbubbles in imaging and therapy: physical principles and engineering. Phys. Med. Biol., 54(6), R27.

Rychak, J.J., Graba, J, Cheung, A.M.Y., Mystry, B.S., Lindner, J.R., Kerbel, R.S. and Foster F.S. (2007). Microultrasound molecular imaging of vascular endothelial growth factor receptor 2 in a mouse model of tumor angiogenesis. Mol. Imaging., 6, 289–296.

 Sboros, V. and Tang, M. X. (2010). The assessment of microvascular flow and tissue perfusion using ultrasound imaging. Proceedings of the Institution of Mechanical Engineers - H, 224(2) 273-290.

Schrope BA, Newhouse VL and Uhlendorf V, 1992. Simulated capillary blood flow measurement using a nonlinear ultrasonic contrast agent. Ultrasonic Imaging 14, pp. 134–158.

Schrope, B., Newhouse, V.L., and Uhlendorf, V. (1992). Simulated capillary blood flow measurement using a nonlinear ultrasonic contrast agent. Ultrasonic Imaging, 14,134–158.

Schrope, B.A., and Newhouse, V.L. (1993). Second harmonic ultrasonic blood perfusion measurement. Ultrasound Med. Biol., 19, 567–579.

Schuster, H.G. and Just, W. (2005). Deterministic Chaos, An Introduction, Wiley-VCH Verlag GmbH and Co. KGaA, Weinheim

Shankar, P.M., Krishna, P.D., and Newhouse, V.L. (1998). Advantages of subharmonic over second harmonic backscatter for contrast-to-tissue echo enhancement. Ultrasound Med. Biol., 24, 395–399.

Shankar, P.M., Krishna, P.D., and Newhouse, V.L. (1999). Subharmonic backscattering from ultrasound contrast agents. J. Acoust. Soc. Am., 106(4),2104-2110.

Shi, W.T., Forsberg, F., and Goldberg, B.B. (1997a). Subharmonic imaging with gas-filled microbubbles (abstract). J. Acoust. Soc. Am., 101, 3139.

Shi, W.T., Forsberg, F., Oung, H. (1997b). Spectral broadening in conventional and harmonic doppler measurements with gaseous contrast agents. Proc IEEE Ultrason Symp 1575–1578.

Shi, W.T., Forsberg, F., Raichlen, J.S., Needleman, L., Goldberg, B.B. (1999). Pressure dependence of subharmonic signals from contrast microbubbles. Ultrasound in Medicine & Biology, 25(2), 275-283.

Simon, G., Cvitanovic, P., Levinsen, M.T., Csabai, I., Horvath, A. (2002). Periodic orbit theory applied to a chaotically oscillating gas bubble in water. Nonlinearity, 15, 25-43.

Sirsi, S., Feshitan , J., Kwan, J., Homma, J., Borden, M. (2010). Effect of Microbubble Size on Fundamental Mode High Frequency Ultrasound Imaging in Mice. Ultrasound in Medicine & Biology, 36(6), 935-948.

Smith, R.A., Cokkinides, V. and Eyre, H.J. (2006). American Cancer Society guidelines for the early detection of cancer. CA. Cancer J. Clin., 56, 11–25.

Sprague M.R., Chérin, E., Goertz, D.E. and Foster S.F. (2010). Nonlinear Emission from Individual Bound Microbubbles at High Frequencies. Ultrasound in Medicine & Biology, 36(2), 313-324.

Sun, Y., Kruse, D.E., Dayton, P.A. and Ferrara, K.W. (2005). High-frequency dynamics of ultrasound contrast agents. IEEE Transactions on Ultrasonics, Ferroelectrics and Frequency Control, 52 (11), 1981-1991

Tang, M.X., and Eckersley, R.J. (2006). Nonlinear propagation of ultrasound through microbubble contrast agents and implications for imaging. IEEE Trans. UFFC, 53, 2406–2415.

Yu, T., Xiong, S., Mason, TJ., and Wang, Z. (2006). The use of a microbubble agent to enhance rabbit liver destruction using high intensity focused ultrasound. Ultrasonics Sonochemistry, 13(2), 143-149.

Weidner, N., Folkman, J., Pozza, F., Bevilacqua, P., Allred, E.N., Moore, D.H., Meli, S., and Gasparini, G. (1992). Tumor angiogenesis: a new significant and independent prognostic indicator in early-stage breast carcinoma. J. Natl Cancer Inst., 84, 1875–1887.

Wickline, S.A. and Lanza, G.M. (2002). Nanotechnology for molecular imaging and targeted theraphy. Circulation, 107, 1092–1095.

Wiesmann, M., Meyer, K., Albers, T., Seidel, G. (2004). Parametric perfusion imaging with contrast-enhanced ultrasound in acute ischemic stroke. Stroke, 35, 508– 513.

Zhang, Y., Cardoso, J.C., Wang, Y., Fish, P.J., Bastos, C.A.C., and Wang, W. (2004). Time-scale removal of "wall thump" in Doppler ultrasound signals: A simulation study. IEEE Trans. Ultrason. Ferroelectr. Freq. Control., 51, 1187–1192.

Zheng, H., Barker, A., and Shandas, R. (2006). Predicting Backscatter Characteristics from Micron- and Submicron-Scale Ultrasound Contrast Agents Using a Size-Integration Technique. IEEE Transactions on Ultrasonics, Ferroelectrics, and Frequency Control, 53(3), 639-644.

Zonderland, H.M., Coerkamp, E.G., Hermans, J., van de Vijver, M.J. and van Voorthuisen, A.E. (1999). Diagnosis of breast cancer: contributions of US as an adjunct to mammography. Radiology, 213, 413–422.